Journal of Applied Geology, vol. 9(1), 2024, pp. 1–25
DOI: http://dx.doi.org/10.22146/jag.87742

Electrical Resistivity Tomography and Boreholes Data to Investigate the Near-Surface Structure under the Campus Area of Çanakkale Onsekiz Mart University, Çanakkale, Turkey (Türkiye)

Nart Coşkun[1], Özcan Çakır*[2], Yusuf Arif Kutlu[3], and Murat Erduran[4]

[1]*Cumhuriyet University, Department of Geophysics, Sivas, Türkiye, nartcoskun@cumhuriyet.edu.tr*
[2]*Süleyman Demirel University, Department of Geophysics, Isparta, Türkiye, ozcancakir@sdu.edu.tr*
[3]*Çanakkale Onsekiz Mart University, Department of Geophysics, Çanakkale, Türkiye, yakutlu@comu.edu.tr*
[4]*MEF Petroleum, Logistics, Construction Company, Ankara, Türkiye, erduranm71@gmail.com*

Received: August 8, 2023 | Accepted: June 17, 2024 | Published online: October 31, 2024

ABSTRACT. We study the soil foundation underneath the Çanakkale Onsekiz Mart University (ÇOMU) campus, Çanakkale, Türkiye, by employing the electrical resistivity tomography – ERT supported by 27 boreholes data. The studied area in the southwest Marmara region was historically affected by large earthquakes (. They were created by the North Anatolian Fault system. The borehole data show that the near-surface structure beneath the ÇOMU campus is mostly silty sands and marls. A high-sensitivity resistivity instrument is used to collect the field data in which nine ERT profiles reaching lengths as long as 315 m are utilized. The current geoelectrical measurements are simulated using two numerical models to estimate the inversion depth sensitivity, which is satisfactory in the depth range of 0-30 m and then somewhat decreasing. The observed electrical resistivity values range from 2–160 Ωm. The geoelectrical structure corresponding to the silty sands is represented by low resistivities (<20 Ωm), while the high resistivity (>40 Ωm) depth sections are associated with the marl units. The resistivity structure beneath the ÇOMU campus is complex, where both low and high resistivity depth sections reside side by side. The groundwater and clay mineralogy contribute to the broad changes in the subsurface resistivities. The groundwater flow below the steep terrain of the ÇOMU campus causes low resistivities (<10 Ωm) deeper than 10 m depth. The borehole data superimposed on the two-dimensional (2-D) ERT profiles show consistency with the resistivity-depth distributions at corresponding depths..

Keywords: Electrical resistivity · Inversion · Landslide · Near surface · Tomography.

1 INTRODUCTION

The Çanakkale Onsekiz Mart University – ÇOMU was founded in 1992 on a 659092 m^2 campus area on the eastern side of the Çanakkale strait (Figure 1a). The ÇOMU buildings and infrastructure are largely built on the hilltop area with rough morphology and an average altitude of 100 m. From west to east, the surface topography is plain up until the ÇOMU campus, which is ~800 m from the Çanakkale strait and then suddenly gains slope over 20°. The slope angle in the N–S direction is milder than in the E–W direction. The ÇOMU is a fast-growing university attracting many students from various countries, which brings up the need to construct more buildings and infrastructure to meet the educational and administrative demands. The near-surface geological stratification in and around the campus area (Neogene-Quaternary – e.g., Gökaşan *et al.*, 2012) is characterized as depositional envi-

*Corresponding author: Ö. ÇAKIR, Süleyman Demirel University, Department of Geophysics, Isparta, Türkiye. E-mail: ozcancakir@sdu.edu.tr

ronments about the formation of the Çanakkale strait (e.g., Yaltırak *et al.*, 2000; Gökaşan *et al.*, 2008). Additional loads on the ground surface due to the increasing number of new buildings and high-intensity traffic may induce slope stability problems and landslides in the campus area (e.g., Cruden & Varnes, 1996). In addition, large earthquakes and aftershocks likely in the region (see Figure 2) may also trigger land moves. These concerns have motivated the current study.

We employ electrical resistivity tomography – ERT (e.g., see Coşkun *et al.*, 2016a) to examine the geological stratification under the ÇOMU campus area. The ERT as a near-surface geophysical method measuring the subsurface resistivity distribution is commonly utilized to investigate the geological conditions related to slope stability problems (e.g., Guo *et al.*, 2005; Drahor *et al.*, 2006; Perrone *et al.*, 2014; Di Giuseppe *et al.*, 2015; Coşkun *et al.*, 2016b; Bentivenga *et al.*, 2019; Bentivenga *et al.*, 2021; Bai *et al.*, 2022; Bentivenga *et al.*, 2022). The ERT method, non-invasive and cost-effective to explore large areas, efficiently delineates the underground properties such as porosity, water content, salinity, clay content, and depth to a layer interface (e.g., Loke, 2004). The ERT method is more efficient in characterizing the geologic framework if integrated with other methods providing diverse data such as geotechnical, borehole, and inclinometer data (e.g., Sudha *et al.*, 2009; Travelletti & Malet, 2012; Chelli *et al.*, 2020). Among the other near-surface geological events, landslides create catastrophic landforms threatening communities worldwide with different influences (i.e., loss of life, property damage, health issues, utility shortages) changing from one location to another. Therefore, developing landslide monitoring strategies should help raise awareness and understanding of landslide hazards in communities (e.g., Li et al., 2020; Thirugnanam *et al.*, 2022). With the advancements in technology in the data collection techniques supported by multiple electrodes, multiple core cables, and multiple arrays, the time-lapse ERT method could be effectively used to monitor unstable slopes (e.g., Xu *et al.*, 2016; Hojat *et al.*, 2019; Lapenna & Perrone, 2022; Dimech *et al.*, 2022).

To our knowledge, the present study includes the first geophysical work performed for the ÇOMU campus area. On the other hand, after careful research, we realized that this area was originally examined in 1994 for geological and geotechnical site characterization. The results were reported to the university administration as a geotechnical field survey (i.e., ÇOMU 1994). However, the submitted report was only made available printed on paper. We acquired this survey report as complete as possible. We digitized it as necessary in the present study—the cited geological field survey comprised 40 cored boreholes located at different locations within the campus area. The boreholes with a 965-m total length were designed to have two different depth penetrations (i.e., 20-m and 30-m). These 15 boreholes had a 30-m total depth, while the remaining 35 boreholes had a 20-m depth penetration. The high slope areas in the campus were examined using the deeper boreholes (i.e., 30 m), while the shallower boreholes (i.e., 20 m) were used to examine the flat or mildly sloped areas. The coring samples (cuttings) were used to identify the geological stratification (lithological units) beneath each borehole location. An in-situ standard penetration test (SPT) was also performed at each well location to determine soil strength through penetration resistance. The city of Çanakkale takes place on the Biga peninsula, which is tectonically influenced by the southern branch of the North Anatolian Fault Zone (NAFZ). The region historically shaken by strong ($M_s \geq 7.0$) earthquakes (e.g., see Şengör *et al.*, 2005; Lai *et al.*, 2021) is prone to earthquake hazards. We combine the geological and geotechnical data (ÇOMU 1994) with the ERT data to better characterize and understand the engineering properties of soil deposits beneath the ÇOMU campus.

We first introduce the earlier geological (drilling and mapping) and geotechnical (SPT) data provided by ÇOMU (1994) and then present the recent fieldwork to collect the apparent resistivities along the selected profiles. The non-linear inversion technique is utilized to invert the collected apparent resistivities for the subsurface resistivity-depth distribution beneath each profile. We perform theoretical tests on two selected models representing the two-dimensional (2-D) electrical resistivities in

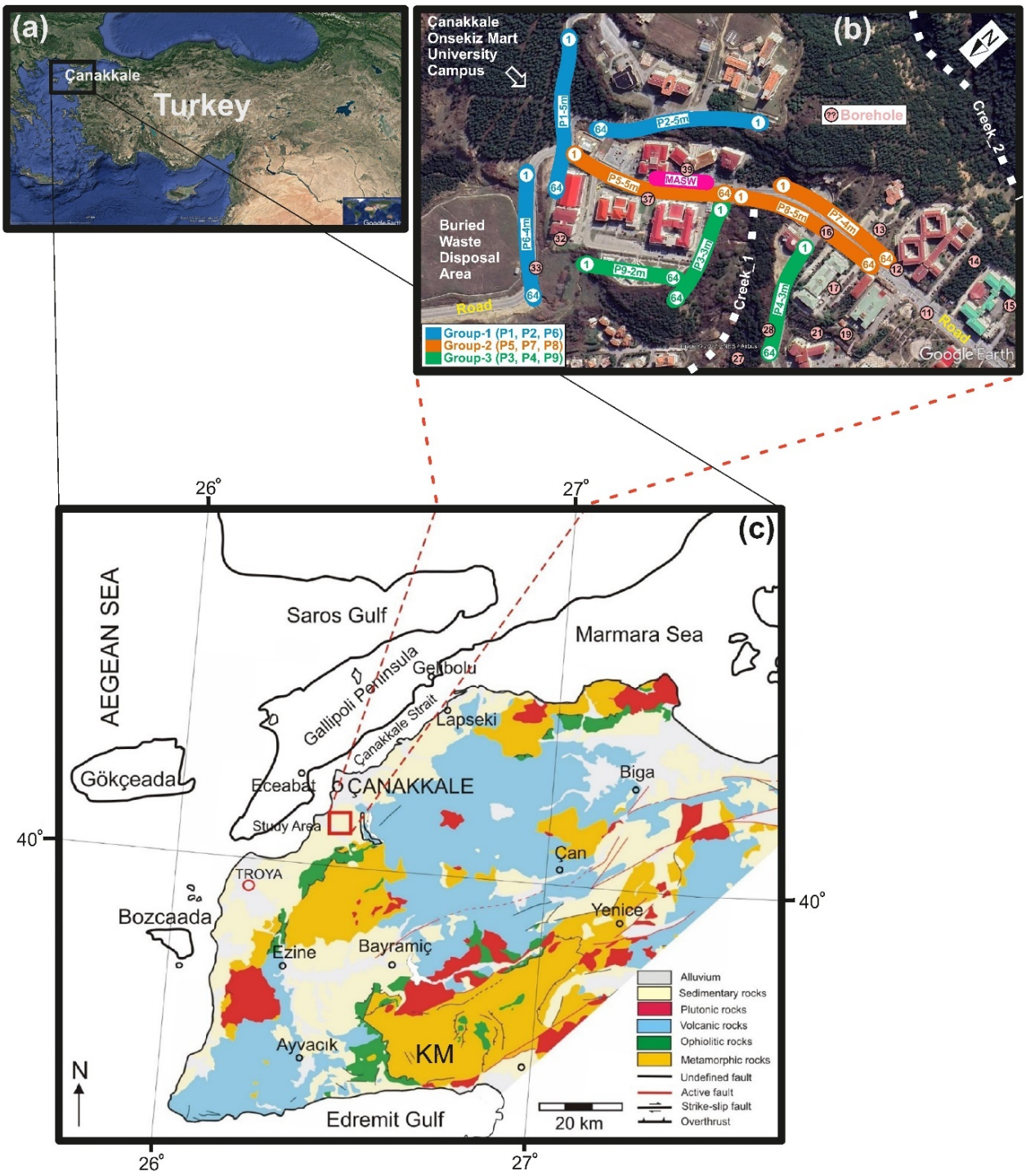

FIGURE 1. Location map (a), electrical resistivity profiles (b), and lithological map of the Biga Peninsula (c) adapted from Coşkun *et al.* (2016b) are shown. A black square on the location map indicates the Biga Peninsula. A red square on the lithological map shows the study area near the city of Çanakkale. KM stands for the Kazdağ Massif. The electrical resistivity profiles depicted by various color (blue, orange, green) lines are superimposed on the Google Earth image. The north axis on the upper right panel (b) is shifted to better visually inspect the study area (ÇOMU campus).

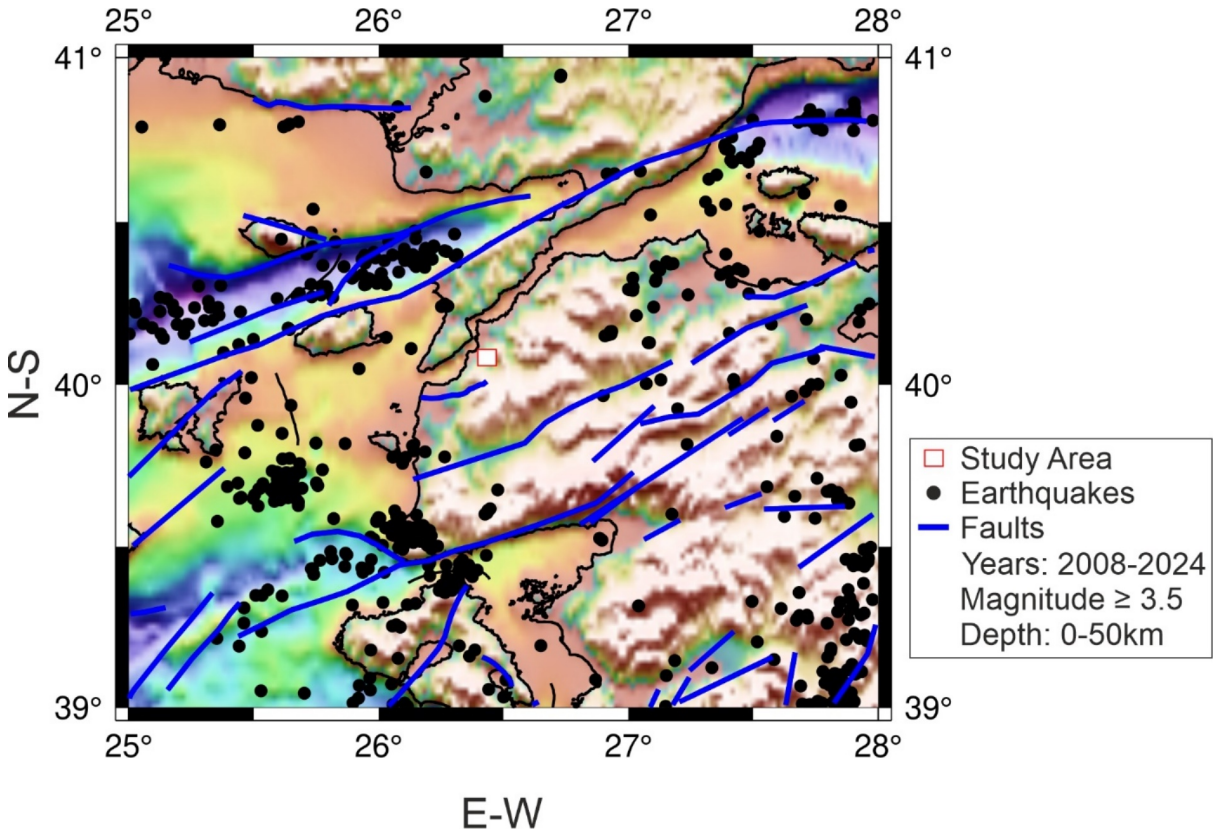

FIGURE 2. Regional seismicity and fault lines are shown (see MTA 2002; Emre *et al.* 2013; Akbas *et al.* 2017; AFAD 2023). Information regarding the earthquake data is summarized on the right.

the shallow (<55 m) earth. These numerical tests are designed to assess the basic resolution power of the observed resistivity data. The resistivity-depth distributions obtained from different profiles are combined to attain the studied area's quasi-three-dimensional (3-D) resistivity image. The borehole data are employed together with the resistivity data to improve the interpretation of the geoelectrical sections for the geological units.

2 GEOLOGICAL BACKGROUND AND REGIONAL CONDITIONS

The city of Çanakkale is located on the Biga Peninsula in NW Turkey, which is a tectonically active region and has been essentially investigated by several workers (Okay *et al.*, 1991; Okay & Satır, 2000; Beccaletto, 2003; Çakır, 2019). The earthquake activity (see Figure 2) is mainly generated by these faults associated with the southern branch of the North Anatolian Fault Zone – NAFZ (Şengör *et al.*, 2005). This region consists of various magmatic, metamorphic, and sedimentary rocks. The study area is located close to the Çanakkale city center. The lithological structure mainly comprises a shallow sequence of Quaternary alluvium deposits, unconsolidated clastic sediments, sand, and gravel blocks (Figure 1c). The average thickness of this formation is between 40–50 m, and its depth decreases towards the east. Most of the geothermal fields on the Biga Peninsula are trending NE–SW along the active faults (Şaroğlu *et al.*, 1992; Emre *et al.*, 2013), which are responsible for the tectonic evolution of the peninsula. Metamorphic, ophiolitic rocks and ophiolitic mélanges form the basement rocks in the Biga Peninsula. The sedimentary and volcanic structures (Late Cretaceous to Neogene) and volcanic and volcano-sedimentary sequences (Late Eocene–Oligocene) generally cover the basement rocks.

In Figure 3b, we show the locations of inactive (or dormant) and active landslides reported for the region along the Çanakkale strait (MTA, 2022). Figure 3a shows the surface geological units in and around the studied area where these fourteen geological units (i.e., U1–U14) are mainly specified. The Kazdağ Massif – KM, characterized by geological units around U6 in

Figure 3a, includes a metamorphic basement (Precambrian-Paleozoic) containing gneiss, amphibolite, and marble. The KM also consists of three formations (ÇOMU, 1994), i.e., Tozlu formation (meta-ultramafic rocks including serpentinized dunites, metagabbro, and amphibolite), Bozağaç formation (biotite, amphibolite, muscovite, sillimanite disten and cordierite gneiss) and Sarıkız formation (thin layered, curly texture, and non-silicate marbles). The Ezine group overlies the Kazdağ group, the Karakaya complex, and the Çamlıca metamorphic rocks (Okay & Satır, 2000; Beccaletto, 2003). The Ezine group (Oligocene granitoids represented by U14 in Figure 3a – Akal, 2013) is bordered by several geological formations, i.e., Middle Miocene rhyolite, dacite, rhyodacite to Miocene terrigenous clastics to Lower-Middle Miocene non-graded volcanites. The Karakaya complex is represented by U10 in Figure 3a (i.e., Upper Paleozoic-Triassic schist, phyllite, marble, metabazic – Okay & Satır, 2000) and is cut through by granitoid intrusions. The Karakaya complex also comprises conglomerate, metagrovac, siltstone, radiolarite, mudstone, Permian-aged various-sized limestone blocks, and greenschist facies metamorphic detrital rocks (ÇOMU 1994). The Çamlıca metamorphic rocks (Palaeozoic schist represented by U5 in Figure 3a – Okay and Satır, 2000) are bordered by undifferentiated volcanics (Oligocene – U1) to the east–northeast and peridotites (Mesozoic – U8) to the west. The Çetmi ophiolitic mélange (U13 in Figure 3a – Upper Cretaceous/Paleocene) in relation to the Biga suture zone consists of strongly altered basaltic rock, limestone, pelagic shale, turbiditic sandstone, blueschist, and minor amounts of serpentine and radiolarian chert (e.g., Okay *et al.*, 1991; Beccaletto *et al.*, 2005; Coşkun *et al.*, 2016b). In the west-northwest, the Biga peninsula is covered by the undifferentiated sediments (Quaternary) and the neritic limestones and continental clastics (Miocene) represented by U9 in Figure 3a. The landward segment of the southern Marmara Sea is covered by terrigenous clastics (Pliocene – U2) and undifferentiated sediments (Quaternary – U3).

The Marmara Sea surrounds the Biga Peninsula in the Marmara region to the north. The Aegean Sea to the west experiences the Mediterranean climate. It is frequently affected by weather conditions developing in Central Europe, i.e., strong winds mostly coming from NW, annual temperatures in the range from -11 to 39 °C with a 19 °C average, occasional snowfall in the winter and average rainfall around 625 mm/year (MGM, 2022). Recurrent rainfalls and earthquakes might initiate landslides in the current region (e.g., Saito *et al.*, 2018). ÇOMU (1994) reported the study area's hydrological characteristics. The plain between the Çanakkale strait and the ÇOMU campus is covered by Quaternary aged alluvial deposits (Figure 1c) where the depth to the underground water table is shallow (1–6 m). Towards the east, beneath the ÇOMU campus, the area is covered by a Neogene sedimentary sequence (sandstone, clay, silt, marl, and limestone), and there is no sign of aquifer water. However, silty sand layers exist sporadically with a small amount of water once used by local people as spring water. There is no surface-water flow Within the study area (i.e., rivers). The rainfall and snowmelt are drained under gravity through the dry valleys aligned roughly in the E–W direction. Further east beyond the ÇOMU campus, the products of andesitic volcanic rocks (Miocene-Pliocene) are intercalated within the sedimentary formations.

Based on the boreholes (40 different locations) and field observations, ÇOMU (1994) has reported that the near-surface lithology of the studied area represents a lacustrine depositional environment (Neogene) and is mostly made of silty sands and marl layers. Intermittently thin layers of sandy, silty clay, clayey, silty sand, silty sandy clay, gravel silty sand, sandstone, clayey silt, silty clay, and sandy silt were also observed. The silty sands with yellow-to-light-brown color, converting to sandy silt at some locations, are mostly fine-grained, but occasionally coarser grain sizes are also noted. The marl unit was reported in ÇOMU (1994) to have various colors changing from red to blue and gray color, relatively lower mechanical strength, and mostly plain texture, though unevenly laminated with minor silt and sand sheets at some locations. In Figure 4, we graphically summarize these lithological units cut at 27 well locations as acquired from ÇOMU (1994). We could not find the cor-

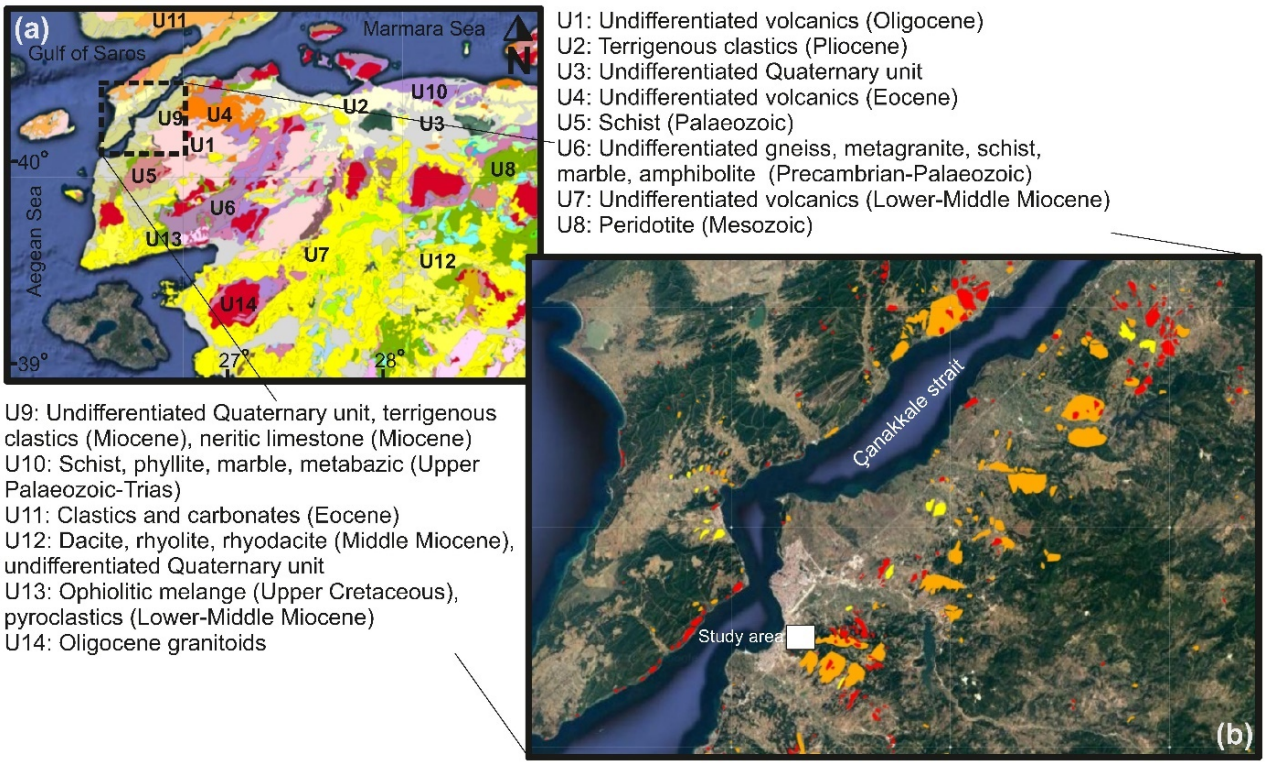

FIGURE 3. Surface geological units in and around the studied area (a) are shown in detail (adapted from Çakır, 2018). The numerals from U1 to U14 superimposed on the map indicate the geological units. The Google Earth image (b) shows the landslides distribution along the Çanakkale strait (MTA, 2022). Inactive (or dormant) and active landslides are indicated by orange and red, respectively.

responding lithological data for the other 13 well locations. In the horizontal axis, the color-coded boreholes are ordered with respect to their number assigned by ÇOMU (1994), while the vertical axis refers to the elevation from the sea level (m). From left to right, the boreholes are approximately ordered from south to north. The two-dimensional (2-D) field locations of the boreholes are shown in Figure 6, along with the locations of the electrical resistivity profiles. The presentation in Figure 4 is dominated by two colors, i.e., cyan color referring to the silty sand and yellow color to the marl lithology.

We present the results of the in-situ standard penetration tests (SPT) conducted by ÇOMU (1994) for some of these borehole locations in Figure 4. In ÇOMU (1994), the SPT hammer blow counts obtained through a standard field procedure (e.g., see Sandikkaya, 2008) were interpreted in terms of the soil strength at different depths (Table 1). Fine-grained soils were reported as stiff or very stiff, while coarse-grained soils were reported as tight or tight. The last hammer blow count (i.e., 26) was obtained for the silty clays. The blow count changed to 37 for the silty sands, 36 for the sandy clayey silts, 33 for the silty sandy clays, and 49 for the marls. The hammer blow count greater than 50 was called refusal. The SPT blow counts are usually utilized to estimate the shear strength properties of soil foundations (e.g., Akin *et al.*, 2011). The marl units show higher mechanical strength for the studied area than the silty sands. The SPT results in Table 1 show that the soil strength beneath the studied area is classified as mostly stiff or medium stiff. The soil strength near the surface graded as soft or very soft was described in a few locations.

There exist field studies conducted in the Çanakkale province, and its surroundings show that the region suffers from a high risk of landslides (e.g., Duman *et al.*, 2006; Dağdelenler *et al.*, 2014; Dağdelenler *et al.*, 2015; Perinçek, 2018). Many active and inactive (or dormant) landslides exist in Çanakkale, especially around the study area (Figure 4b). These areas of high elevation mainly show signs of old and new landslides, as evidenced by scarp faces, soil de-

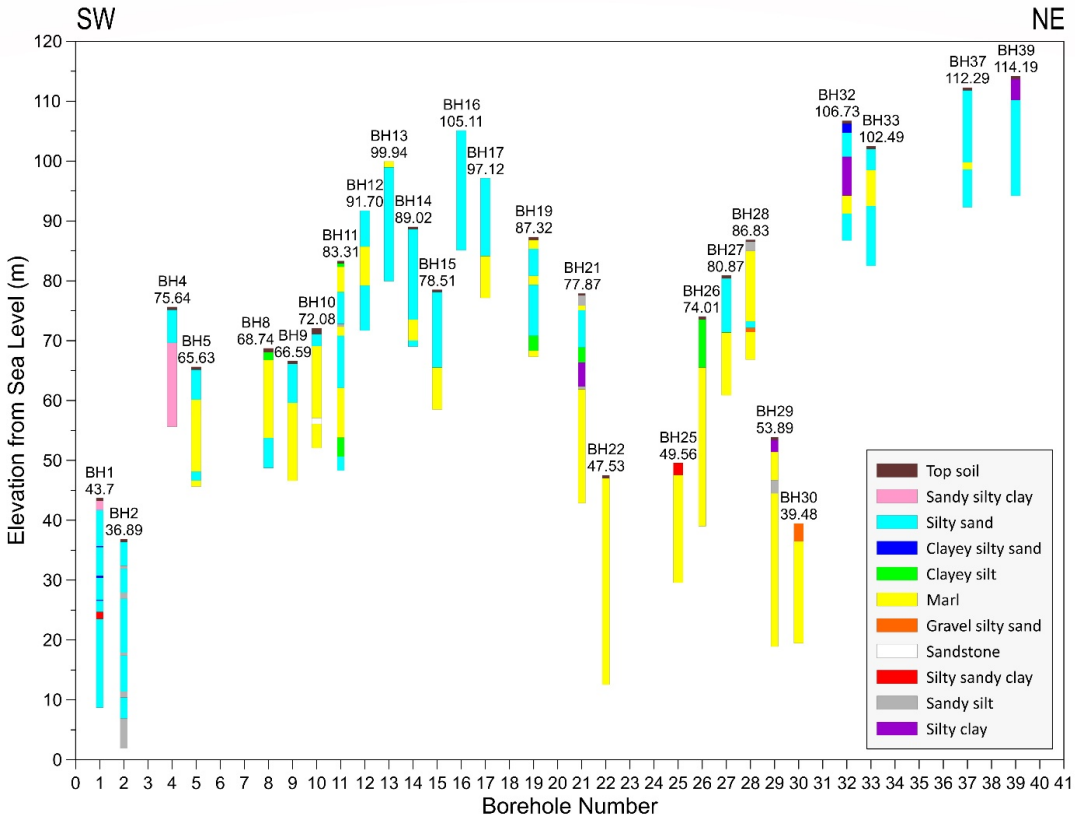

FIGURE 4. Boreholes and lithology identified from cuttings acquired from ÇOMU (1994) are shown. The borehole number and elevation (m) from the sea level are indicated on top.

bris, fragmented rock falls, and erosional landmarks (e.g., Perinçek, 2018). The regional topography on both sites of the Çanakkale strait is constantly reshaped by landslides developing on mostly east-west facing slopes. In Figure 5, we provide a map view of the studied area utilizing a Google Earth image on which some regions are marked using different color lines. The yellow line encircles a large area corresponding to the ÇOMU campus. Next to the ÇOMU campus, there is another area surrounded by the Blue Line, which is an old solid waste dumpsite used by Çanakkale Municipality for many years until it was abandoned and gradually rehabilitated starting the year 2004 (e.g., Sağlık *et al.*, 2021). The area surrounded by the red line represents the terrain earlier examined by Coşkun et al. (2016b) for a landslide risk assessment using the ERT method. These purple lines, inside and outside the ÇOMU campus, indicate areas of sharp elevation change down the slope towards the Çanakkale strait. As indicated by green color arrows, most campus buildings occur on the eastern (uphill) side of the purple lines. The traffic between the cities of Çanakale and İzmir uses the highway indicated in Figure 5 where, following the 1915 Çanakkale Bridge Highway Project, the traffic load on this highway, along with traffic-induced vibrations, is considerably increased.

3 DATA AND METHOD

Electrical resistivity tomography – ERT is employed to assess the resistivity-depth distributions beneath two-dimensional (2-D) profiles where the measurements are made on the ground surface (Figure 1b). Since the study area is a university campus, we have experienced some difficulties in the field while selecting the profile locations. The campus buildings, roads covered by brick and asphalt, concrete bases for street lampposts, and natural vegetation frequently prevented us from picking these profiles with proper lengths and locations. However, we still managed to measure the apparent resistivity values of the subsurface along nine 2-D profiles. Figure 6 illustrates these 2-D profiles (blue, orange, and green color lines). We had to allow the profiles to deviate from the linearity depending on the field measure-

TABLE 1. Standard penetration test (SPT) results obtained in situ at different depth levels (ÇOMU 1994). The borehole number and depth (m) are given in the first column. A comma separates multiple depth intervals in the second column.

Borehole	Depth Intervals (m)	Soil Strength
BH1 – 30 m	1.5-1.95, 9.5-9.62	Medium Stiff
	9.0-9.45, 16.5-16.95	Medium Stiff
BH2 – 30 m	19.0-19.5	Stiff
	30.0-30.45	Medium Stiff
BH5 – 20 m	9.50-9.62, 15.0-15.1	Medium Stiff
BH8 – 20 m	1.5-1.95, 4.5-4.87, 12.0-12.45	Medium Stiff
	18.0-18.3	Stiff
BH9 – 20 m	1.5-1.95, 4.5-4.95, 8.0-8.1, 15.0-15.1, 18.0-18.19	Medium Stiff
BH10 – 20 m	1.5-1.95, 9.0-9.45, 13.5-13.6, 16.5-16.72, 20.0-20.3	Medium Stiff
BH11 – 30 m	6.0-6.11, 9.0-9.13	Medium Stiff
BH12 – 20 m	3.05-3.13, 7.5-7.87, 10.55-10.85	Medium Stiff
BH13 – 20 m	1.6-1.81, 15.0-15.1, 18.0-18.3	Medium Stiff
BH14 – 20 m	1.5-1.6	Stiff
	17.4-17.5	Medium Stiff
	1.5-1.6	Soft
BH15 – 20 m	5.4-5.5	Medium Stiff
	13.5-13.6, 17.0-17.5, 19.0-19.7	Stiff
BH16 – 20 m	9.0-9.3, 14.0-14.07, 18.0-18.2	Medium Stiff
BH17 – 20 m	1.50-1.95	Soft
	10.5-10.7, 13.5-13.8, 16.5-16.7, 19.9-20.0	Medium Stiff
BH19 – 20 m	1.5-1.95	Very Soft
	3.0-3.32, 19.9-20.0	Medium Stiff
	4.65-4.97, 6.0-6.22	Medium Stiff
BH21 – 30 m	10.5-10.56	Stiff
	15.0-15.2, 24.0-24.01	Medium Stiff
BH22 – 30 m	1.0-1.1, 3.5-3.62, 7.5-7.62	Stiff
	15.5-15.6, 25.5-25.6	Medium Stiff
BH25 – 20 m	1.5-1.6	Stiff
	5.5-5.61, 9.5-9.6, 13.5-13.55, 19.5-19.57	Medium Stiff
	1.50-1.95	Medium Stiff
BH26 – 30 m	6.45-6.5	Soft
	13.5-13.8, 18.0-18.1	Medium Stiff
BH27 – 20 m	11.6-11.75, 16.5-16.58	Medium Stiff
BH29 – 30 m	4.0-4.5	Stiff
	16.5-16.6, 27.0-27.1	Medium Stiff
BH30 – 20 m	1.55-1.7	Stiff
	4.5-4.58	Medium Stiff
BH32 – 20 m	7.5-7.8, 10.5-10.8	Medium Stiff
BH33 – 20 m	5.50-5.95	Stiff
	1.20-1.5	Medium Stiff
BH39 – 20 m	3.0-3.22	Stiff
	19.9-20.03	Medium Stiff

ment conditions. The ERT profiles are chosen to broadly cover the studied area where some profiles come close to each other, but no intersection between profiles occurs. In the field, we used a constant scheme of 64-electrode data collection where the electrode spacing was kept variable (i.e., 2-m, 3-m, 4-m, and 5-m). Considering the average electrode spacing (i.e., 3.5 m), the total profile length is 220.5 m, yielding a depth penetration of around 55 m, about one-fourth of the electrode spread length. The shortest profile (i.e., Profile 9) used the 2-m electrode spacing with a total profile length of 126 m, while these longest profiles (i.e., Profiles 1, 2, 5, and 7 with a total profile length of 315 m) utilized the 5-m electrode spacing. On the other

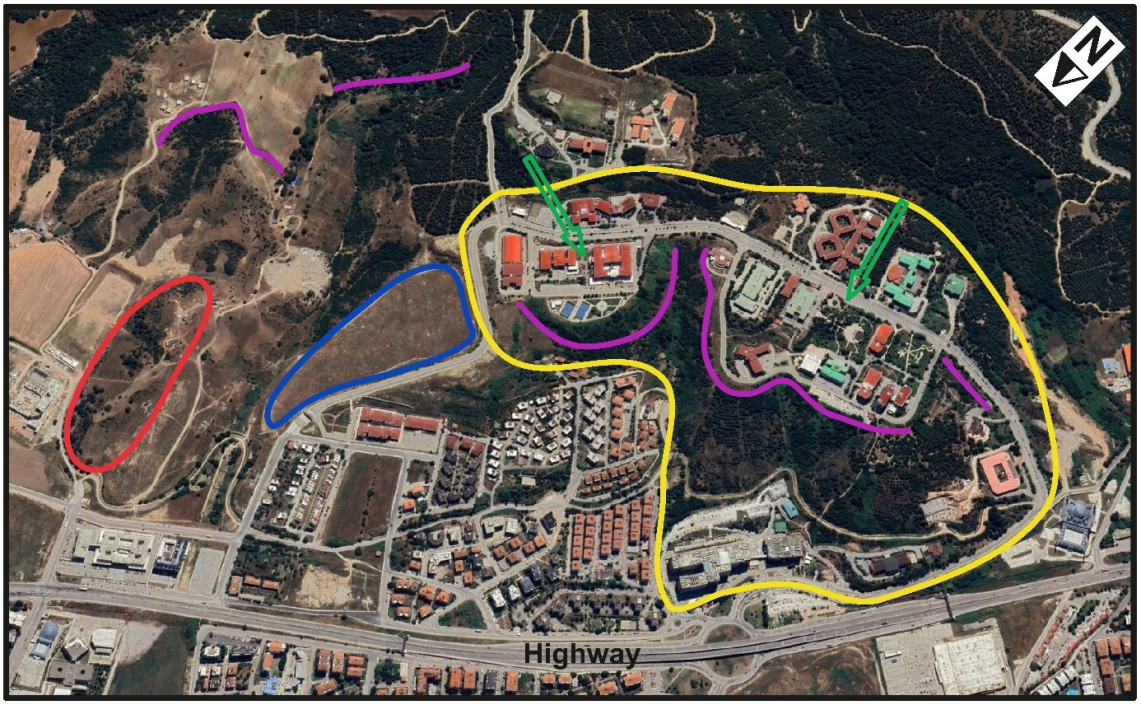

FIGURE 5. The study area (closed yellow line) and its vicinity are shown on a Google Earth image. The closed red line to the left indicates the area studied by Coşkun *et al.* (2016b). Çanakkale Municipality once used the location stated by the closed blue line for solid waste disposal. Purple lines show these likely landslide scarps. The highway links the cities of Çanakkale and İzmir.

hand, Profiles 3 and 4 used the 3-m electrode spacing, and in Profiles 6 and 8, a 4-m electrode spacing was utilized.

In Figure 6, we show some borehole locations indicated by borehole numbers within circles with a pink background. These boreholes drilled by ÇOMU (1994) take place in the close vicinity (i.e., a few five meters) of the electrical resistivity profiles currently measured. In Figure 6, we also show the location of a seismic profile conducted by AFAD (2023). This seismic profile (marked as MASW) extending parallel to the last half of the fifth electrical resistivity profile (i.e., P5 in Figure 6) is indicated by cyan color. It takes place almost in the middle of the studied area. AFAD (2023) deployed a new accelerogram station (40.1129°N, 26.4221°E with 1714 station code and 128-m altitude) starting December 13, 2013. The station deployment location was examined for near-surface geophysical properties using a nearby seismic profile along which MASW (e.g., see Xia *et al.*, 1999) and REMI (e.g., see Cox & Beekman, 2011) surface wave measurements were taken. The subsequent measurements were inverted to obtain the one-dimensional (1-D) shear-wave (Vs) velocity-depth distribution beneath the 48-geophone spread accompanied by a 50-kg weight drop, 2-m offset, and 2-m geophone interval. Figure 7 shows the respective results where the surface wave phase velocity inversions are illustrated in three different colors, i.e., MASW inversion (blue color), REMI inversion (green color), and MASW plus REMI joint inversion (red color). The MASW and REMI inversions show somewhat different 1-D Vs profiles, particularly below the 25-m depth. The latter is most likely the result of various data collection techniques utilized by the MASW and REMI methods in the field. Figure 7 shows that in the depth range 0-15 m, the Vs velocity is around 350 m/s and then changes to ~500 m/s in the depth range 15-30 m. AFAD (2023) has reported that the average Vs30 velocity is around 429 m/s and that the soil foundation underneath the new accelerogram station 1714 is graded B according to Ec8 (Eurocode). In Figure 7, the lithological units cut through the BH39, which takes place close (~10-m) to the MASW profile, are superimposed on the illustration. The relatively higher velocities in the depth range of 0–4 m correspond mainly to

FIGURE 6. The ÇOMU campus and the electrical resistivity profiles indicated by orange lines are shown on a Google Earth image. Superimposed on the profile is the profile number and electrode spacing. The first (1) and last (64) electrodes are also specified. The seismic profile, which is a magenta color, indicates MASW. The two-digit borehole numbers are printed within circles with a pink color background.

the silty clays, while the deeper parts (4–20 m) are represented by the silty sands in which the shear-wave (Vs) velocities tend to increase below ~14-m depth. Karagöz (2022) has reported that the shear-wave velocities within the area relevant to the ÇOMU campus are slower than 800 m/s in the 0-100 m depth range.

We collect the ERT data using an automated system equipped with full wave-shaped electrical data collection, which is a multi-channel (61 channels), multi-core cable, and multi-electrode (64 electrodes) system, i.e., ZZ Geo FlashRes64 resistivity instrument (e.g., Adhikari *et al.*, 2016; Coşkun *et al.*, 2016b; Ross *et al.*, 2019; Su *et al.*, 2021). This instrument is free of traditional (e.g., dipole-dipole, Wenner, or Schlumberger) or any other complex electrode arrays (see user's manual, e.g., Coşkun *et al.*, 2016a and 2016b). Instead, a mixture of all possible current (AB) and potential (MN) electrode configurations is used to collect the field data. In the FlashRes64 system, any two electrodes are used to inject the electrical current into the ground. Then, all the remaining electrodes are used to measure the N-3 voltages for each electrode spread, where N is the number of electrodes. The data corresponding to various multi-electrode configurations (ABMN) are eventually combined into a singular dataset used in the inversion. The 61-channel capability of the FlashRes64 system allows fast collection of large amounts of data, which substantially increases the resolution of the geoelectrical inversion beneath the survey line, i.e., better identification of the vertical and lateral changes of the subsurface electrical resistivities in tomography studies.

3.1 Numerical Tests

We consider two model structures representing the near-surface (<55 m) 2-D distribution of electrical resistivities. The respective model structures are displayed in Figure 8 (upper rows). They represent a two-layer model with some heterogeneities embedded in the first layer. Below the 30-m depth (i.e., second layer), the geoelectrical structure is assumed constant at 300 Ωm. Above the 30-m depth, the resistivity distribution is considered to have a checkerboard pattern made of three depth levels, which is a test procedure frequently utilized in seismic wave propagation problems to assess the resolution power (e.g., see Chen *et al.*, 2010; Fang *et al.*, 2016; Çakır, 2019). Each cell in the

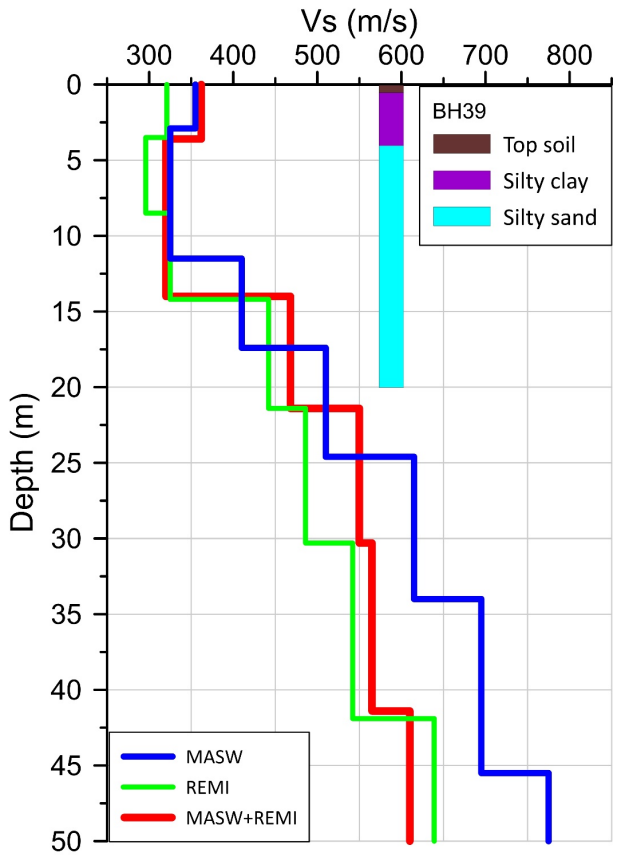

FIGURE 7. One-dimensional shear-wave (Vs) velocity-depth distribution underneath the seismic profile indicated as MASW in Figure 6. Borehole data (BH39) is shown superimposed in the respective depth range. See the main text for more explanation.

checkerboard pattern is assumed to have 10 m thickness and 25-m length. The background resistivity is set to 100 Ωm. In contrast, three anomalous structures with high and low resistivities (i.e., 20 Ωm, 50 Ωm, and 200 Ωm) defining the checkerboard pattern are assumed to partly change the background structure. Figure 8 shows these anomalous structures with resistivity values (Ωm) printed in white. These two test models are different from each other in the depth range shallower than 30 m. The first model (left panel in Figure 8) is assumed to have an anomalously high resistivity of 200 Ωm in the 0–10 m depth range. In comparison, for the same depth range, the second model (right panel in Figure 8) has an anomalously low resistivity of 20 m. The second-level anomalies in the depth range of 10–20 m are represented by two different resistivity values, i.e., 50 Ωm (first model) and 200 Ωm (second model). In the third level, the first model anomalies have the lowest resistivity value (20 Ωm) in the depth range of 20–30 m, where the second model is represented by 50 Ωm.

The theoretical calculations (apparent resistivities and inversions) emulating the field procedures are performed using the open-source software – ResIPy by Blanchy *et al.* (2020). Several modeling parameters such as electrode spacing, mesh generation (triangular or quadrilateral), and electrode array, as well as forward modeling (e.g., Dai *et al.*, 2021), inversion (e.g., Perrone *et al.*, 2014), and plotting are provided through a graphical user interface – GUI and Python application programming interface – API. The measured resistivities corresponding to the theoretical subsurface are assumed to be observed by 64 electrodes with 3.5-m electrode spacing (black dots along the surface in Figure 8), which is the average of electrode spacing currently applied in the field, i.e., 2-m, 3-m, 4-m and 5-m. The subsurface (rectangular anomaly shapes and a flat layer) is digitized via the triangular meshing (upper row in Figure 8). The triangular meshing becomes coarser with depth because the sensitivity to the geoelectrical structure decreases with increasing depth. Multiple electrode arrays (i.e., Schlumberger, Dipole-Dipole, Wenner, and Multi-Gradient), as shown in Figure 9, are simultaneously employed to measure the electrical response of the subsurface. The Schlumberger array with a=2 and n=30 is represented by 870 quadrupoles in the apparent resistivity pseudo section. The number of quadrupoles for the Wenner array with a=21 is 651. 870 quadrupoles represent the Dipole-Dipole array with a=2 and n=29. The Multi-Gradient array with a=2, n=61, and s=61 is defined by the highest number of quadrupoles, i.e., 18445. When these electrode arrays (i.e., Schlumberger, Dipole-Dipole, and Multi-Gradient) in Figure 9 are re-arranged with a=1, then the number of quadrupoles is almost doubled, which means better resolution of the subsurface, but this many quadrupoles require computational time (CPU) and memory (RAM) beyond our current computing capabilities. Therefore, we abandon the case of a=1 and only share the resolution analysis achieved by a=2.

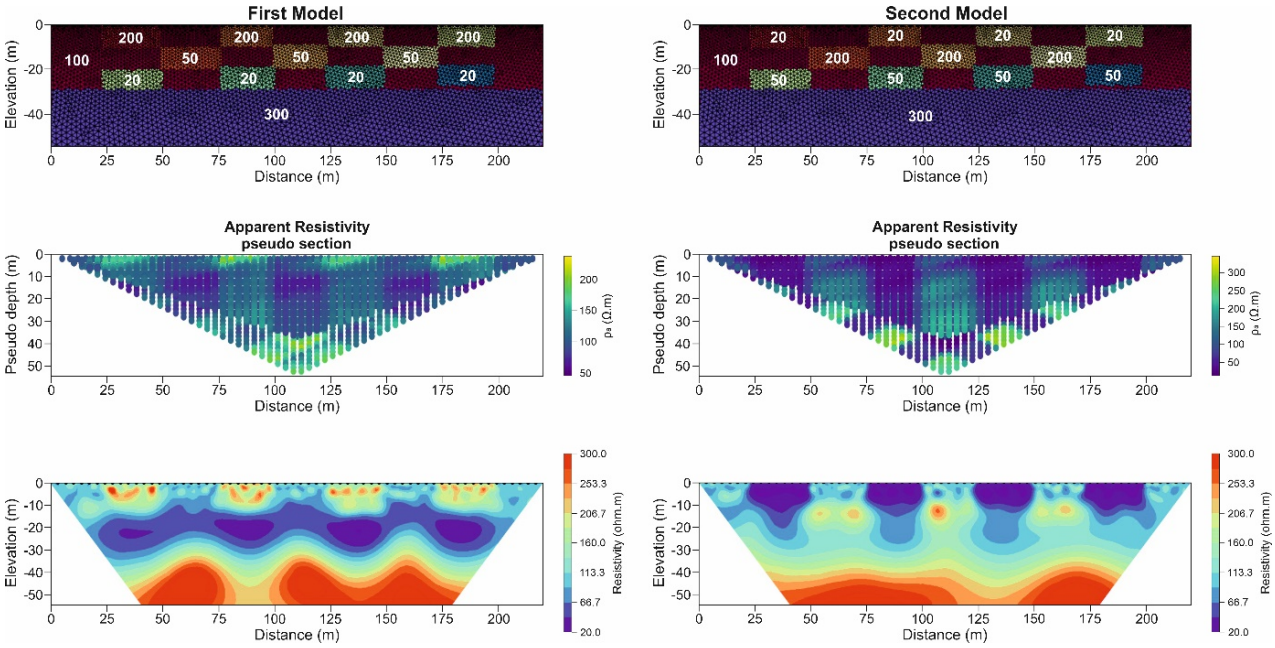

FIGURE 8. Two theoretical models are shown to assess the resolution of the electrical resistivity tomography (upper row). The middle row displays the corresponding apparent resistivity pseudo sections. The inverted resistivities for the true resistivity values in the upper row are shown in the lower row.

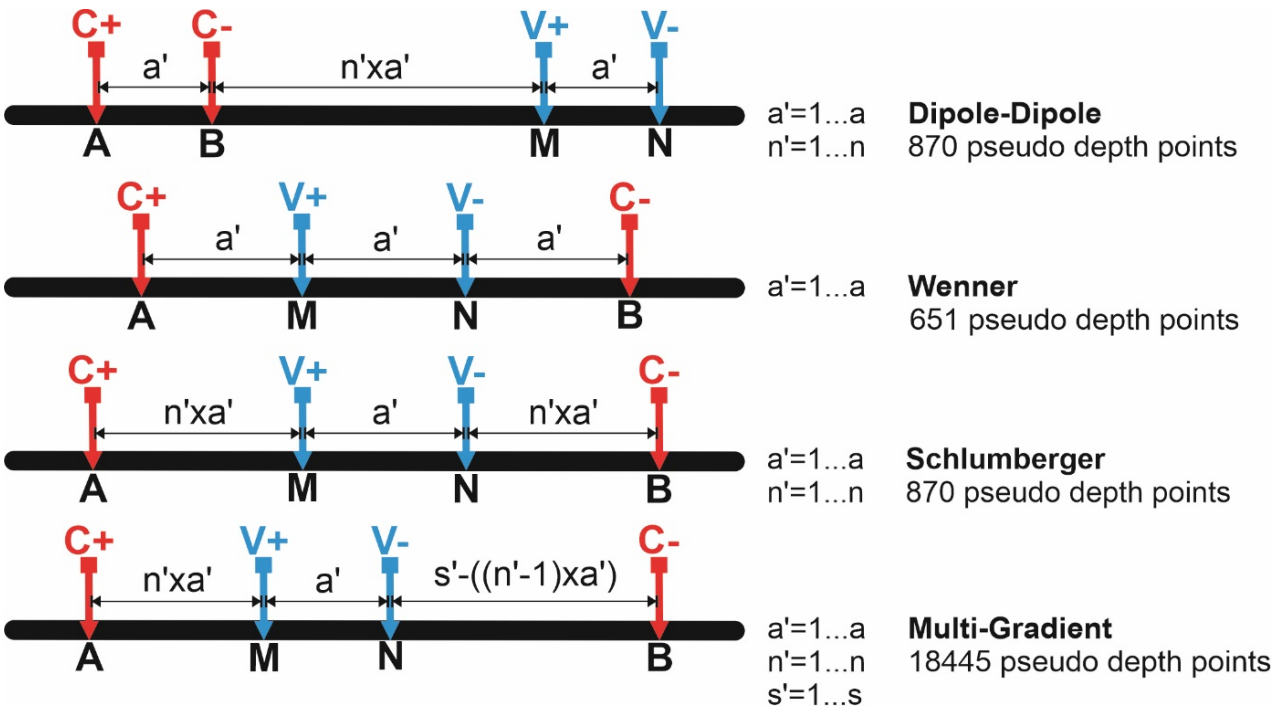

FIGURE 9. Electrode arrays used in electrical resistivity tomography are shown. Electrical current is introduced into the subsurface using current electrodes A and B, and the voltage difference is measured via M and N potential electrodes. The geometrical relationship between current and potential electrodes is designed according to free parameters (a, n, s) shown alongside each array.

The middle row in Figure 8 shows the 2-D apparent resistivity values corresponding to each model structure in the upper row, where the computations are performed under random noise (3%) conditions. The evident resistivity pseudo-sections (middle row) obtained after forward modeling of the model structure with 20836 pseudo-depth points are inverted to recover the true resistivity depth sections, as shown in the lower row in Figure 8. A rainbow color scale is applied to illustrate how the inverted resistivities vary with depth, where the high and low resistivities are depicted in red and blue color tones, respectively. The inversion results in Figure 8 reveal how efficiently the ERT can resolve the near-surface resistivity variations and depth to the homogeneous layer underlying the above heterogeneous structure. The inverted resistivities in Figure 8 (lower row) show that the near-surface structures are better resolved, and then the resolution power gradually decreases with increasing depth. The electrical currents traversing the subsurface have high intensity near the surface (e.g., see Çakır & Coşkun, 2021). Therefore, the shallow structure is better resolved in the inversion, i.e., with a smaller resolution radius (e.g., see Friedel, 2003). For deeper investigation, the spacing between the current electrodes is increased so that the electrical currents have greater depth penetration. However, at increasingly greater depths, the apparent resistivity is influenced by a larger volume of subsurface material, increasing the resolution radius (Friedel, 2003). The latter case results in the poor resolution of deeper structures.

The inverted resistivities corresponding to the first and second models in Figure 8 (lower row) show that the checkerboard pattern with three levels in the depth range of 0–30 m is satisfactorily resolved. These anomaly structures with high (200 Ωm) and low (20 Ωm) resistivities are relatively well isolated from the background structure at 100 Ωm. Still, the other anomaly structure with 50 Ωm is not well resolved and somewhat mixes with the background structure. Even though the electrical resistivity within each abnormal structure in the checkerboard pattern is modeled homogeneous, the inverted resistivities, especially those near the surface, show some fluctuations in the range of 10–50 Ωm around the true resistivity values. The rectangle shape of each anomaly is relatively poorly imaged on the inverted cross sections since the inverted resistivities do not precisely resolve the edges. Despite the inversion problems mentioned above, the anomaly structures corresponding to the checkerboard pattern are still visible on the inverted cross-sections. The layer interface at 30-m depth defines a resistivity jump from low resistivity (100 Ωm) to high resistivity (300 Ωm). The checkerboard pattern in the third level alters this resistivity jump. In the first case model (left panel in Figure 8), the jump occurs in the range of 20-to-300 Ωm, and this range changes to 50-to-300 Ωm for the second model (right panel). The inverted resistivities relating to the first model (lower row in left panel) properly reflect the layer interface's topography created by the checkerboard pattern. Still, the interface depth is predicted to be ~5-m deeper than the actual value (30 m). A gradual increase replaces the corresponding resistivity jump with depth. The half-space resistivity (300 Ωm) becomes evident only at depths greater than 40-m. The case with the second model (lower row in right panel) regarding the layer interface develops differently. The lateral variation on the interface topography created by the checkerboard pattern is less obvious, and the half-space resistivity (300 Ωm) becomes visible at even greater depths (>45-m). The resistivity change replacing the resistivity jump at 30-m depth is even more gradual. The nonuniform conductivity distribution within the Earth determines the actual current flow. The near-surface structure comprising a layer with high conductivity or low resistivity may create a short-circuit effect, permitting fewer electrical currents to reach greater depths (e.g., Milsom, 2003). The low resistivity (20 Ωm) segment in the depth range of 0–10 m in the second model in Figure 8 appears to suffer from this short-circuit effect.

4 INVERSION RESULTS AND DISCUSSIONS

There are nine profiles along which we conducted electrical resistivity tomography – ERT. We divide these nine profiles into three groups to analyze the subsequent findings effectively. The first group is made of profiles 1, 2, and 6, which are profiles covering mostly the eastern

section of the ÇOMU campus (blue color profiles in Figure 6), and these three profiles taking place in the second group (i.e., orange color profiles 5, 7 and 8) extend along the road connecting the two parts of the campus area (see Figure 6 and green color arrows in Figure 5). The third group profiles (i.e., green color profiles 3, 4, and 9) cover mostly the northwestern part of the campus where a creek (Creek_1 – Figure 6) takes place between profiles 3 and 4. In the next section, we interpret the boreholes (Figure 4) and the ERT profiles.

4.1 Profiles 1, 2 and 6

Group-1 profiles (blue color profiles in Figure 6) are made of profiles 1, 2, and 6, where profiles 1 and 6 extend with identical directions (NW–SE) whi, and profile 2 runs perpendicular (NE-SW) to the first two profiles in this group. Figure 10 displays the 2-D electrical resistivity inversion results corresponding to Group-1 profiles where the 2-D cross sections are approximately placed on the display according to their positions in the field—profile 6 starts covering the region from the point where profile 1 ends. Profiles 1 and 2 have the same electrode spreading (i.e., 315-m length with 5-m electrode spacing), while profile 6 is the shortest in this group with 252-m length and 4-m electrode spacing. The topography significantly changes in the studied area and is therefore considered in the current resistivity inversions. The maximum depth range is set to 60 m below which the inversion depth sensitivity significantly diminishes (see discussions in Figure 8). Each ERT profile in Figure 10 has its rainbow color scale. The 2-D resistivity inversions are color-coded from dark red (high resistivities – HR) to light blue (low resistivities – LR). The highest resistivities (around 140 Ωm) are observed below profile 1 (see color scale P1), while the subsurface below profiles 2 and 6 shows relatively lower resistivity values (<50 Ωm – see color scales P2 and P6). Some depth sections underneath Group-1 profiles are represented by lower resistivity values (<10 Ωm – see all color scales). Figure 10 indicates high resistivity zones (HRZ) and low resistivity zones (LRZ). Not all HRZs and LRZs are marked on the figure to prevent clutter on the illustration. Still, the color coding helps visualize how these high and low resistivity depth sections are distributed underneath Group-1 profiles.

The borehole data presented in Figure 4 reveal that the relevant geology near the surface (<30 m) is made of sedimentary units, mostly marl and silty sands. Based on this information, we interpret that the high resistivity zones (HRZs) in Figure 10 correspond to the marl units, which are mechanically stronger and probably drier. We also interpret that the low resistivity zones (LRZs) arise from the silty sands, which are mechanically weaker with probably some water content. The clay mineral contained in the marl and silty sands, as well as silty clays, sandy, clayey silts, and silty sandy clays, may have the effect of lowering the observed resistivity values, which correspond to these depth sections represented by the color range from blue to yellow in the color scales (Figure 10).

4.2 Profiles 5, 7 and 8

In Figure 11, we show the ERT results for Group-2 profiles (orange color profiles in Figure 6), which are made of profiles 5, 7, and 8. A four-lane road runs through the ÇOMU campus (see Figure 6), along which Group-2 profiles with approximately E–W direction are utilized to survey the subsurface. Profile 8 starts covering the region from where Profile 5 ends, and Profile 7 runs parallel to Profile 8, which is approximately 30 m apart towards the north. In this group, profiles 5 and 8 have the same electrode configuration (i.e., 315 m length with 5 m distance between electrodes), while profile 7 has the shortest length (i.e., 252 m) with 4-m electrode spacing. Similarly to Figure 10, the 2-D ERT cross sections are placed on the display according to their estimated positions in the field. The rainbow scale from dark red (high resistivities – HR) to light blue (low resistivities – LR) represents the resistivity-depth distribution underneath Group-2 profiles. However, for profile 5, we apply an exception where the color scale is designed to run from yellow (HR) to light blue (LR) to visualize the resistivity-depth distribution beneath profile 5 better. Otherwise, the other details of the respective 2-D cross section (particularly low resistivities) are obscured by the HRZ around 80-m distance and 20-m depth.

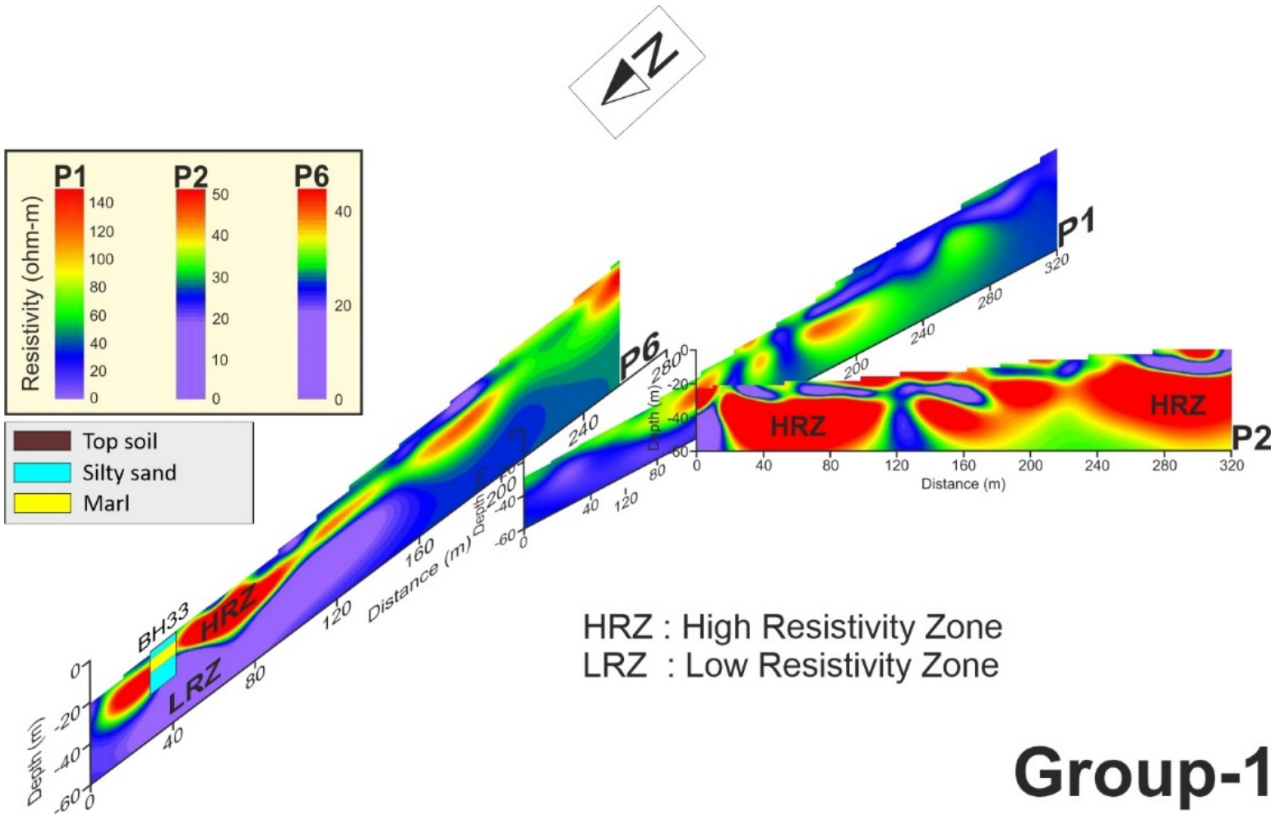

FIGURE 10. Group 1 profiles surveying the E–NE part of the ÇOMU campus are shown along with the lithological legend and north – N direction. The profile length reflects the horizontal scale on the resistivity cross sections.

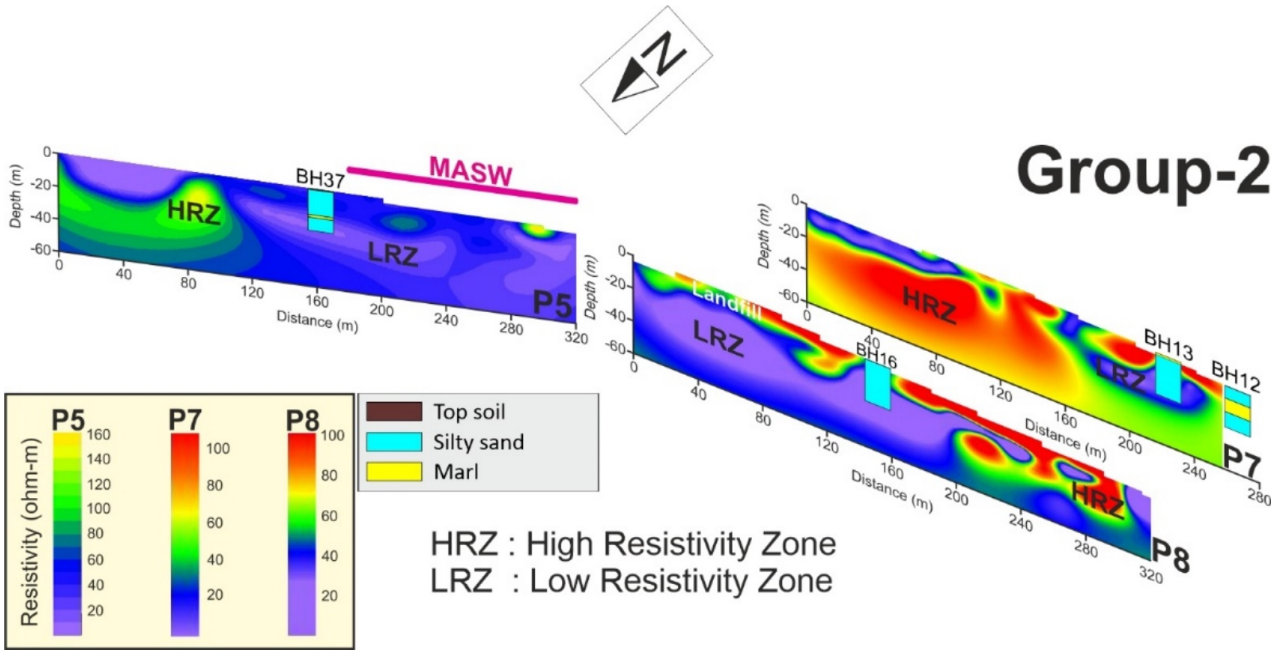

FIGURE 11. Group 2 profiles surveying the central part of the ÇOMU campus. The legend, including the horizontal scale and N direction, is shown in Figure 10.

The highest resistivities (around 160 Ωm) are observed below profile 5 (see color scale P5), while the subsurface below profiles 7 and 8 shows relatively lower resistivity values (<100 Ωm – see color scales P7 and P8). Some depth sections underneath Group 2 profiles represented by the light blue color correspond to even lower resistivity values (<20 Ωm – see all color scales). In Figure 11, we again identify these high (H) and low (L) resistivity zones (RZ). Not all HRZs and LRZs are indicated in the figure to avoid confusion in the illustration. The color coding helps visualize how these HRZs and LRZs are distributed underneath Group 2 profiles. The near-surface depth section marked as landfill in profile 8 is explained in the next section. Like the interpretation of Figure 10 based on the borehole data in Figure 4, we consider that the HRZs and LRZs in Figure 11 are mostly characterized by the sedimentary units of marls and silty sands, respectively.

There exists a seismic profile (called MASW – see Figure 6) along which MASW and REMI measurements were taken (AFAD, 2023). Figure 7 presents the respective results of the phase velocity inversions for the shear-wave velocity-depth profiles. This seismic profile running parallel to the ERT profile 5 (thick magenta color line in Figure 11) is placed away from profile 5 at ~25-m distance towards the southeast. The inverted seismic velocities represent the seismic structure near the second half of profile 5, where the ERT inversions show lower electrical resistivities, which we consider corresponding to the silty sands indicated by the BH39 (see Figure 7 and depth section marked LRZ in profile 5). Note that this level of silty sand continues underneath profile 8 at about the same depth range from 20 m to 40 m. However, the latter depth range is replaced by higher electrical resistivities underneath profile 7 (i.e., depth section marked HRZ in profile 7), which we consider to represent a lithological change to the marl unit towards the south. Of course, we rely on the borehole data summarized in Figure 4 to interpret the lithology.

4.3 Profiles 3, 4 and 9

The ERT results for Group-3 profiles (green color profiles in Figure 6), which are made of profiles 3, 4, and 9, are shown in Figure 12. This group of profiles measuring the NW part of the ÇOMU campus is the shortest among the other profiles we measure. Because of inefficient field conditions, we had to set shorter profile lengths for Group-3 measurements—profiles 3 and 4 employ 3-m electrode spacing, corresponding to 189-m profile length and 50-m inversion depth. Profile 9, with 2-m electrode spacing, 126-m length, and 30-m inversion depth, is the shortest in this study. A creek between profiles 3 and 4 is marked as Creek_1 in Figures 5 and 11. We could not take measurements inside this creek because of the steep landscape and heavy vegetation.

In Figure 12, the 2-D ERT cross sections belonging to Group-3 profiles are similarly positioned on the presentation concerning their projected positions in the field. Profiles 3 and 4 have the field positions quite separated (~150 m), while profiles 3 and 9 are relatively closer (see Figure 6). The inverted resistivity depth distribution underneath profile 4 shows significant differences from that underneath profile 3, located on the other side of Creek_1. For instance, in the distance range 0–60 m, profile 3 shows a high resistivity zone. In contrast, for the same distance range, profile 4 indicates a subsurface electrical structure characterized by a mixture of high (>40 Ωm) and low (<10 Ωm) resistivities. The electrical resistivity structure beneath profile 9 looks more like a three-layer structure in which the corresponding layers have the resistivities in a sequence of high (>50 Ωm), low (<20 Ωm), and high (20–50 Ωm) from top to bottom. The color scales in Figure 12 (i.e., P3, P4, and P9) show that the subsurface underneath the Group-3 profiles is represented by relatively lower electrical resistivities, like those obtained underneath profiles 2 and 6 among the Group-1 profiles (see Figure 10). Like the cases presented in Figures 9 and 10 above, we interpret these HRZs and LRZs in Figure 12 as due to the geoelectrical structures related to the sedimentary units of marls and silty sands, respectively.

4.4 Individual Profiles

This section interprets the ERT 2-D cross sections and the boreholes data. Unfortunately, the current 2-D ERT profiles and the boreholes

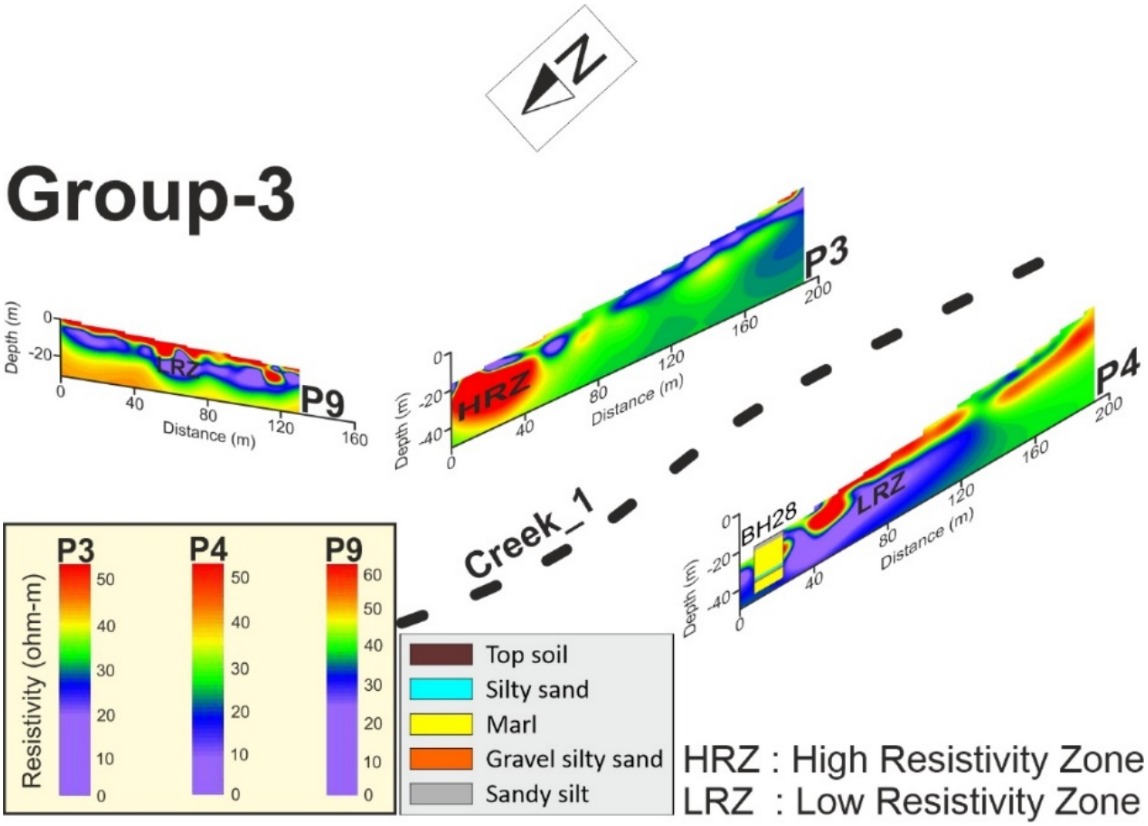

FIGURE 12. Group 3 profiles surveying the NW part of the ÇOMU campus. The same design for the legend, including horizontal scale and N direction, is used in Figure 10.

(ÇOMU, 1994) utilized in this study mostly do not align along the same line. However, we still have a few boreholes (i.e., BH12, BH13, BH16, BH28, BH33, and BH37) located at 0-10 m distances from the 2-D ERT profiles (see Figure 6). We project the corresponding borehole data onto the nearby ERT profile for our structural interpretation. In Figure 13, five individual ERT profiles (i.e., profiles 4, 5, 6, 7, and 8) are interpreted together with the relevant borehole data.

Profile 4 (P4), which is examined first in Figure 13, has an intersection with the BH28 around a 15-m distance where the near-surface geology (0–20 m) is mostly characterized by marl units for which the ERT indicates high resistivities (>40 Ωm). Profile 5 (P5), next in the list, shows an intersection with the BH37 around 160-m distance. The relevant borehole data indicates mostly silty sands within the first 20 m from the surface. At the same time, for the same depth range, the ERT inversion shows electrical resistivities in the range of 30–50 Ωm, which gets even lower (<20 Ωm) for depths deeper than 20-m. Profile 6 (P6) also has an intersection with a borehole (BH33), which occurs around a 40-m distance. Within the 0–20 m depth range, the BH33 shows a three-layer structure (two silty sands and one marl layer), excluding the topsoil within the first 0.5-m. The top and bottom layers of silty sands are characterized by low resistivities (<20 Ωm), and the middle layer of marl is represented by high resistivities (>40 Ωm). Note that the electrical resistivity of a depth section is evaluated as either high or low based on the geoelectrical structure specific to the 2-D ERT cross-section.

Profile 7 (P7) is considered next in Figure 13. The BH13 takes place close to profile 7, around a 220-m distance. There is an altitude difference of 2 m between profile 7 and BH13, reflected in the illustration (see BH13 in Figure 13). The geology within the first 20-m depth range is mostly silty sands (see Figure 4). For the relevant depth range, the 2-D ERT shows low resistivities (<30 Ωm) consistent with the lithology of silty sands. The BH12 is also close to profile 6, around 265-m distance. The 2-D ERT and the three-layer geology (i.e., in order of silty sand, marl, and silty sand) indicated by BH12

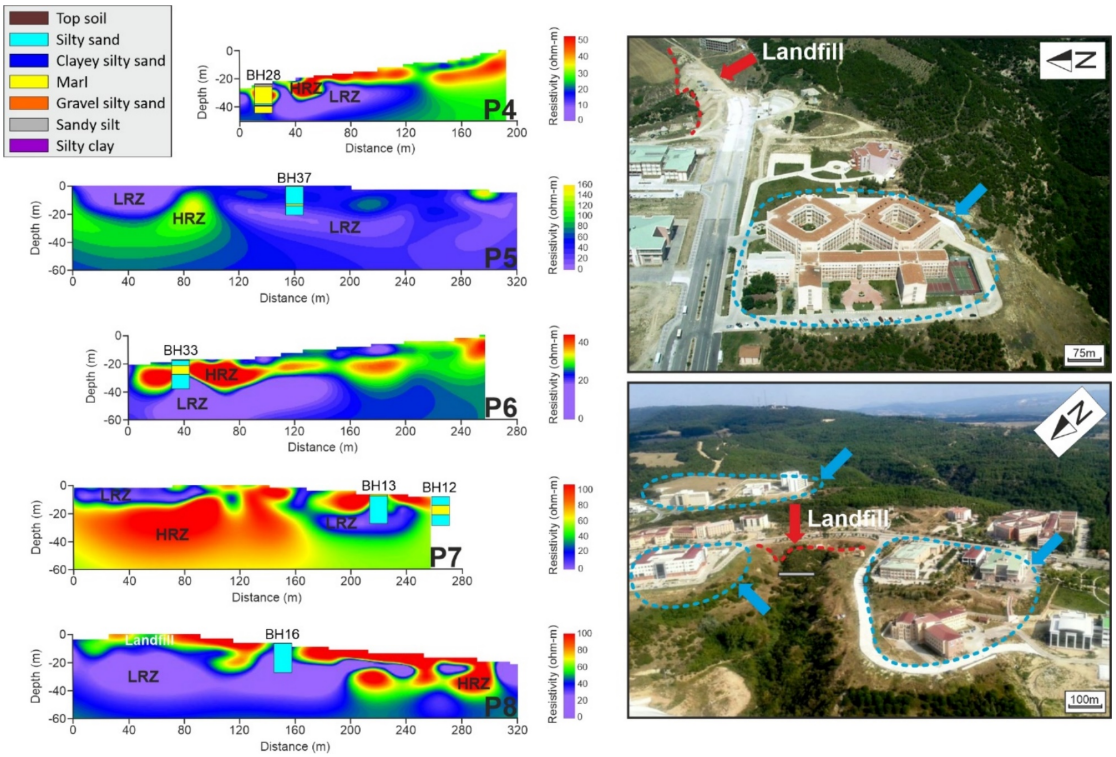

FIGURE 13. Two-dimensional ERT cross-sections on the left are evaluated using the borehole data. Two photographs on the right show the ÇOMU campus viewed from different angles. The blue arrows indicate that the flat landscape is preferred for campus buildings. The lithological legend, horizontal scale, and N direction are shown.

do not exhibit consistency. At the end of profile 7, around 250 m distance, the geoelectrical structure shows resistivities greater than 80 Ωm within the topmost 10 m, and then the resistivity structure becomes less resistive (30–60 Ωm) for the depths deeper than 10 m. The depth ranges near the two profile ends are poorly resolved in the 2-D ERT inversion because of the lower density of electrical currents traversing this part of the geoelectrical structure (e.g., see Naudet et al., 2004). Therefore, profile 7, which has a low resolution around 250 m distance, shows the latter inconsistency with the BH12.

The last profile examined in Figure 13 is profile 8, which intersects with the BH16 and is characterized as having a lithology of silty sands within the depth range of 0–20 m (see Figure 4). For the equivalent depth range, profile 8 showing low resistivities (<20 Ωm) is consistent with the geology revealed by the BH16. The upper end of Creek_1 separates the two parts (E–NE and W–SW) of the ÇOMU campus (see Figure 6), which are indicated by the blue arrows in Figure 13. A road built on the landfill connects the separated campus areas, as shown by the red arrow in Figure 13. The landfill printed in the white color is measured as a high resistivity (>60 Ωm) depth section within the topmost 8-m in the distance range of 10–140 m along profile 8. Below the landfill, the geoelectrical structure is represented by the low resistivities (<25 Ωm), which relates to the silty sands based on the boreholes data utilized herein.

4.5 Pseudo Three-Dimensional Interpretation

The current ÇOMU campus covers an area of over 659092 m^2. A smaller part of the ÇOMU area, around 500×600 = 300000 m^2, is studied in the present work. All the 2-D ERT profiles shown together in the upper row in Figure 14 indicate that the geoelectrical structure underneath the ÇOMU campus is quite complex. The electrical resistivities measured along nine 2-D ERT profiles are as low as 2 Ωm and as high as 160 Ωm. The low resistivity depth sections are correlated with the silty sands, while the high resistivities are interpreted as resulting from the marl units. The clay mineralogy was persistent in much of the geological units (i.e., sandy, silty

clay, clayey, silty sand, clayey silt, silty sandy clay, and silty clay) along with some water content is considered to yield these middle range resistivities taking place between the silty sands and marl units. The middle range resistivities appear to change from one profile to another, e.g., ~40–100 Ωm (P1), ~20–40 Ωm (P2), ~30–70 Ωm (P7) or ~25–45 Ωm (P9). There exist some areas in the campus where the low resistivities (<15 Ωm) cover almost all the depth ranges from the surface down to 40–50 m depths (e.g., see profiles 5 and 8). On the other hand, for some ERT profiles (e.g., profiles 4 and 6), the latter low resistivity depth sections are overlain by some 5–15 m thick high resistivity (i.e., >40 Ωm) depth sections. For some other parts of the ÇOMU campus area, the ERT profiles are largely dominated by high resistivity (i.e., >50 Ωm) depth sections (e.g., profiles 2 and 7) where the geoelectrical structure near the surface is partly represented by the low resistivities (<20 Ωm).

The middle row in Figure 14 displays all the borehole data (i.e., lithological units with increasing depth) that we acquired from ÇOMU (1994). There are 27 boreholes in the figure covering much of the ÇOMU campus except the area indicated by a black arrow where the boreholes are sparse. In the illustration, the depth scale is exaggerated five times (i.e., 1:5) to emphasize the lithological units in boreholes. The near-surface geology underneath the ÇOMU campus mainly comprises silty sands and marl. The layer of silty sand covers the top, and the marl unit underlies it. These two layers have thicknesses that change broadly throughout the campus area. The 20-m deep boreholes (i.e., BH13, BH16, BH37, and BH39) drilling into the high elevation of the ÇOMU campus reveal the topmost cover (i.e., silty sands). Below this cover, we think the marl unit, which is buried deeper, takes place (i.e., see BH14, BH15, and BH5). For the lower altitudes, since the overlying silty sands were largely eroded, the boreholes mostly cut through the underlying marl unit (i.e., see BH22, BH25, BH26, BH28, BH29 and BH30). Part of the campus area showing a steep slope representing the rise of the land surface from approximately west to east (Figure 6) is intercalated by silty sands and marls with varying thicknesses (i.e., see BH8, BH9, BH10, BH11, BH12, BH17, BH19, BH21, BH27, BH32, and BH33). Other lithological units such as clay, gravel, and sandstone also contribute to the layering, but their effect is secondary. We evaluate that the erosion of higher peaks, transportation via Creek_2 (upper row in Figure 14), and deposition was responsible for the generation of silty sands and sandy, silty clays indicated by the three boreholes drilling into the low elevation of the ÇOMU campus to the west (i.e., see BH1, BH2, and BH4).

In the lower row in Figure 14, we attempted to interpret the near-surface structure by interconnecting the geological units between adjacent boreholes, which provides a pseudo-three-dimensional (3-D) engineering geology model of the studied area. The high elevation of the ÇOMU campus is mostly underlain by silty sands (cyan color units). The geological stratification shifts to include mostly marls (yellow color units) in the low-elevation areas of the campus to the west. Note that the 2-D ERT profiles (i.e., P5 and P8) shown in the upper row (Figure 14) imply that the silty sands in the high elevation of the ÇOMU campus extend much deeper than that revealed by the boreholes (i.e., BH13, BH16, BH37, and BH39) in the lower row. In addition, the 2-D ERT profiles (i.e., P4 and P6) in the upper row show that the high resistivities (>40 Ωm) near the surface (likely marl unit) shifts to low resistivity (<20 Ωm) structure (likely silty sands) in the low elevation of the ÇOMU campus. We predict that the low resistivities in the subsurface deeper than 10–15 m depth, indicated by the orange arrows in the upper row, are further lowered (<10 Ωm) by underground waters flowing below ground under the force of gravity acting on the steep slope. The boreholes (i.e., BH21, BH22, BH25, BH26, BH27, BH28, BH29, and BH30) drilling around this area do not have sufficient depth penetration (<20 m) to reveal the details regarding these low resistivity depth sections (see P4 and P6 around 40-m distance in Figure 13). The field observations and the relevant inversions show that electrical resistivity tomography – ERT can broadly resolve the subsurface in the horizontal and vertical directions. This approach should prove more beneficial and be supported by additional data (geological like boreholes and geophysical like seismic observations).

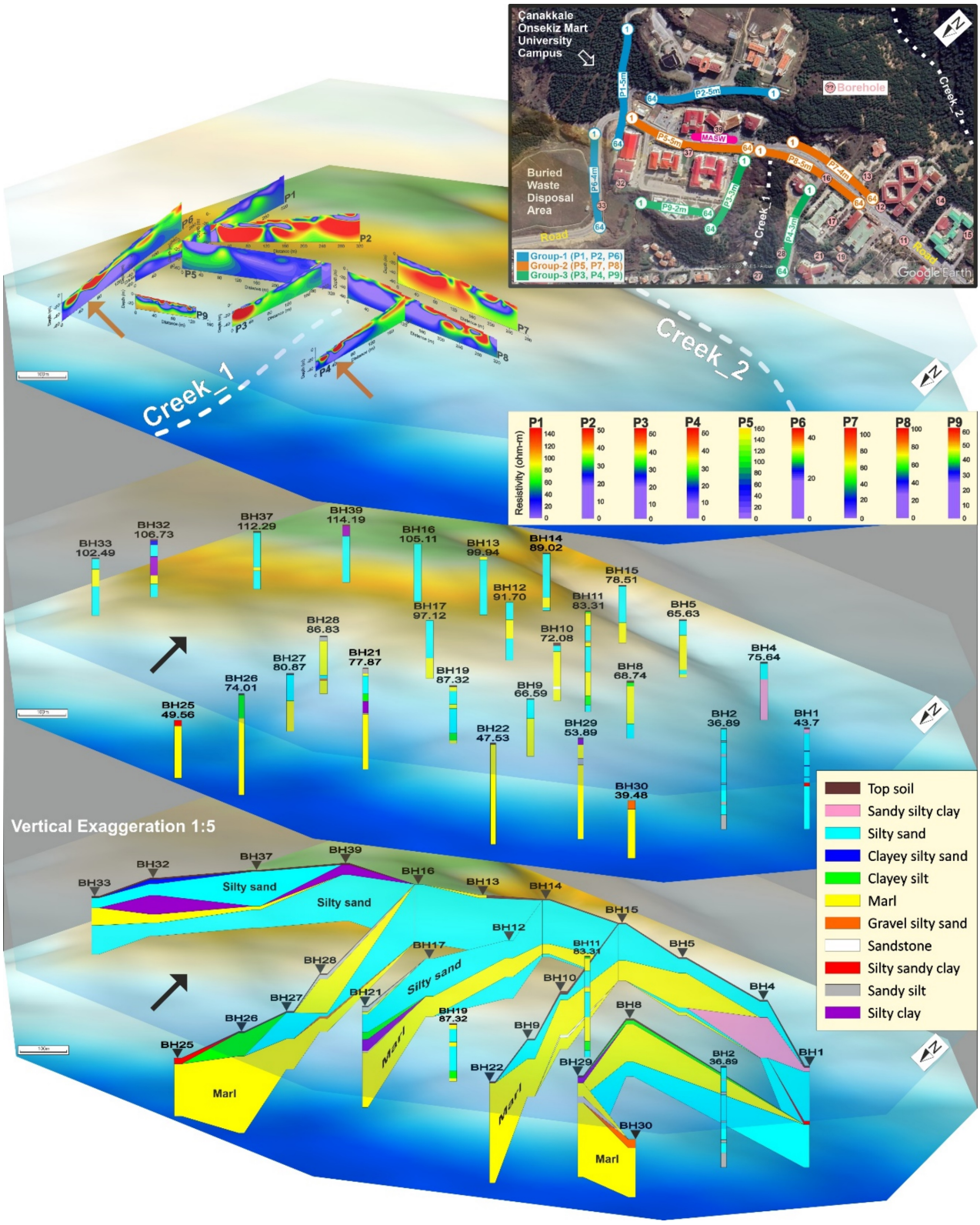

FIGURE 14. Pseudo 3-D presentation of electrical resistivity profiles (upper row) and boreholes data (middle row) provided by ÇOMU (1994) are given along with the horizontal scale and N direction. The lower row demonstrates the structural interpretation of interconnected lithological units between the boreholes. In the middle and lower rows, 1:5 vertical exaggeration is used. The topmost Google Earth map is inserted to display the locations of electrical resistivity profiles. The lithological legend is indicated.

5 CONCLUSION AND RECOMMENDATIONS

With a complex faulting system, the Marmara region in NW Türkiye has historically experienced many destructive earthquakes with surface wave magnitudes greater than 7.0 (e.g., see Altınok *et al.*, 2003). The city of Çanakkale place in SW Marmara was lately struck by the Şarköy-Mürefte earthquake (Ms 7.3) in 1912, where the aftershocks were reported to last about two months (Altınok *et al.*, 2003). The Çanakkale Onsekiz Mart University (ÇOMU) campus taking place in this seismically high-risk region (MTA, 2023) is currently considered in terms of the characteristics of the soil foundation, which is made of a sequence of mostly silty sands and marls. We evaluate that the layer of silty sands partly saturated by underground waters may experience block moves during possible large earthquakes and aftershocks in the region. Mitigation efforts for lowering the pore water pressure and increasing the material shear strength below particularly steep terrain of the ÇOMU campus should be beneficial. We cannot effectively differentiate between groundwater and clay content, for which, in a follow-up study, we recommend the integration of ERT with induced polarization – IP (e.g., see Shao *et al.*, 2021). The groundwater flow may be a significant issue for the ÇOMU campus area for which self-potential – SP can be employed along with other geophysical methods (e.g., seismic) to outline the groundwater flow. In this context, creating an aquifer model of the studied area might be favored, but we do not currently have sufficient data other than the ERT profiles to fulfill such an objective. Herein, we aim to interpret the subsurface in terms of the structure rather than the lithology. For instance, significant electrical differences exist between profiles P2 and P7 (high resistivity) and P5 and P8 (low resistivity). Such structural differences in resistivities may indicate a possible boundary along a fault line as the region is cut by several fault zones (see Figure 2). However, we again do not have enough data to make assertions regarding the fault zone deformations. A more comprehensive approach, including several geological and geophysical methods (especially seismic methods), should prove beneficial for the accurate identification of the aquifer structure and fault zones beneath the respective area.

Recommendations:

The two large Turkish earthquakes on February 6, 2023 (Kahramanmaraş-Pazarcık, and Elbistan,) They have caused massive devastation in Turkey (Türkiye) and Syria. Eleven large cities in SE Türkiye and part of NW Syria have suffered many deaths and economic losses. Thousands of buildings were either destroyed or left uninhabitable. On the brink of time, millions of people were left homeless. Centuries-old monuments (mosques, churches, castles) from diverse backgrounds (Greeks, Romans, Arabs, Ottomans) were heavily damaged by these large earthquakes. All these painful experiences have once more taught us that necessary measures must be taken beforehand to protect the communities against soil liquefaction. The study of the material properties of soils is very important to understand the soil behavior under heavy shake loading. The principles of foundation engineering utilizing the ground survey data obtained from geophysical, geological, and geotechnical studies must be strictly followed in the building construction. The Turkish plate and the surrounding area are still in the process of geological development, and similar large earthquakes will continue to occur. Since the fault system in the region is very complex, one large earthquake triggering another large one in the close vicinity should be expected. Therefore, people must take the necessary steps to reduce the risk of future disastrous earthquakes.

We have followed from social media that some moderate-size aftershocks (i.e.,) caused landslides in the earthquake-hit area. These Kahramanmaraş-Pazarcık and Elbistan earthquakes came about 9 hours apart, and thousands of aftershocks in two to three weeks followed. We interpret that the soil foundation in the region constantly deteriorated due to periodic aftershocks and became increasingly vulnerable to land moves. Then, even moderate-sized aftershocks were able to trigger landslides. On the other hand, the rebuilding processes (i.e., building new homes and infrastructures and restoring cultural heritage) have already begun in this precious region, home

to diverse communities. However, assessing the earthquake risks (faults/fractures, velocity structure, and seismic motions) is essential, and then strictly following the ground improvement rules for soil stabilization. These efforts should be supported by ground surveys (geophysical, geological, and geotechnical) so that the region can be rebuilt more sustainably, which requires constructing the structures to resist the heavy seismic loads. In this respect, the study of electrical resistivity tomography (ERT), a non-invasive geophysical approach applied herein, should be quite effective in helping determine the soil characteristics underneath an area of interest in three dimensions (3-D). The ERT equipment can be moved to different locations in the studied area so that extensive coverage in both vertical and lateral imaging of the subsurface is possible.

Acknowledgements The anonymous reviewers are thanked for critically reviewing the manuscript. The undergraduate students at Çanakkale Onsekiz Mart University, Geophysical Engineering Department, are thanked for helping with the fieldwork. This work was partially supported by the project FAY-2014-337 provided by Çanakkale Onsekiz Mart University.

REFERENCES

Adhikari P.K., Yadav P.K., Srivastava S., Maurya V.P., Singh S., Tripathi A., Singh R.K., & Bage A.K. (2017). Near-surface high-resolution imaging of a metallogenic zone in the northern fringe of Dalma volcanic in eastern India using electrical resistivity tomography. *Exploration Geophysics*, 48, 394-400.

AFAD (2023). Technical details of AFAD (Turkish Disaster and Emergency Management) accelerogram station 1714 (in Turkish), Last visited February 06, 2023.

Akal C. (2013). Presence of coeval shoshonitic–ultrapotassic dyke emplacements within the Kestanbol Pluton, Ezine-Biga Peninsula. *Turkish Journal of Earth Sciences*, 22, 220–238.

Akin, M. K., Kramer, S. L., & Topal, T. (2011). Empirical correlations of shear wave velocity (Vs) and penetration resistance (SPT-N) for different soils in an earthquake-prone area (Erbaa-Turkey). *Engineering Geology*, 119, 1-17.

Altınok, Y., Alpar, B., & Yaltırak, C. (2003). Sarköy-Mürefte 1912 Earthquake's Tsunami, an extension of the associated faulting in the Marmara Sea, Turkey. *Journal of Seismology*, 7, 329–346.

Bai, D., Lu, G., Zhu, Z., Zhu, X., Tao, C., & Fang, J. (2022). Using Electrical Resistivity Tomography to Monitor the Evolution of Landslides' Safety Factors under Rainfall: A Feasibility Study Based on Numerical Simulation. *Remote Sensing*, 14, 3592.

Beccaletto L. (2003). Geology, correlations and geodynamic evolution of the Biga Peninsula, Northwest Turkey. Dissertation, University of Lausanne.

Bentivenga M., Giocoli A., Palladino G., Perrone A., & Piscitelli S. (2019). Geological and geophysical characterization of the Brindisi di Montagna Scalo landslide (Basilicata, Southern Italy). Geomatics, Natural Hazards, and Risk, 10, 1367-1388.

Bentivenga M., Bellanova J., Calamita G., Capece A., Cavalcante F., Gueguen E., Guglielmi P., Murgante B., Palladino G., Perrone A., Saganeiti L., & Piscitelli S. (2021). Geomorphological and geophysical surveys with InSAR analysis applied to the Picerno earth flow (southern Apennines, Italy). *Landslides* 18, 471–483.

Bentivenga M., Gizzi F.T., Palladino G., Piccarreta M., Potenza M.R., Perrone A., Bellanova J., Calamita G., & Piscitelli S. (2022). Multisource and Multilevel Investigations on a Historical Landslide: The 1907 Servigliano Earth Flow in Montemurro (Basilicata, Southern Italy). *Land*, 11, 408.

Çakır Ö. (2018). The seismic crust structure beneath the Aegean region in southwest Turkey is caused by the radial anisotropic inversion of Rayleigh and Love surface waves. *Acta Geophysica*, 66, 1303-1340.

Çakır Ö. (2019). Love and Rayleigh waves are inverted for a vertical transverse isotropic crust structure beneath the Biga Peninsula and the surrounding area in NW Turkey. *Geophysical Journal International*, 216, 2081–2105.

Çakır Ö., & Coşkun N. (2021). Theoretical Issues with Rayleigh Surface Waves and Geoelectrical Method Used for the Inversion of Near Surface Geophysical Structure. *Journal of Human, Earth, and Future*, 2, 183–199.

Cox, B.R., & Beekman, A.N. (2011). Intramethod Variability in ReMi Dispersion Measurements and Vs. Estimates at Shallow Bedrock Sites. *Journal of Geotechnical and Geoenvironmental Engineering*, 137, 354–362.

Chen Y., Badal J., & Hu J. (2010). Love and Rayleigh Wave Tomography of the Qinghai-Tibet Plateau and Surrounding Areas. *Pure and Applied Geophysics*, 167, 1171–1203.

Chelli A., Francese R., Petrella E., Carri A., Quagliarini A., Segalini A., Caporicci M.P., Diena M., Giorgi M., & Celico F. (2020). A multiparameter field monitoring system to investigate the dynamics of large earth slides–earth flows

in the Northern Apennines, Italy. *Engineering Geology*, 275, 105780.

ÇOMU (1994). Jeoloji Mühendislik Sondaj Taah. Tic. ve San. Ltd. Şti., Çanakkale 18 Mart Üniversitesi Yeni Kampüs Alanı Sondajlı Etüd ve Jeoteknik Değerlendirme Raporu. Cilt 1, ÇOMÜ Rektörlüğü, Yapı ve Teknik İşleri Daire Başkanlığı, 17 Sayfa. (In Turkish).

Coşkun N., Çakır Ö., Erduran M., Kutlu Y.A., & Yalçın A. (2016a). Preliminary investigation of underground settlements of Nevşehir Castle region using 2.5-D electrical resistivity tomography: Cappadocia, Turkey. *Arabian Journal of Geosciences*, 9, 717.

Coşkun N., Çakır Ö., Erduran M., Kutlu Y.A., & Çetiner Z.S. (2016b). A potential landslide area investigated by 2.5D electrical resistivity tomography: a case study from Çanakkale, Turkey—*Arabian Journal of Geosciences*, 9, 6.

Cruden D.M., & Varnes D.J. (1996). Landslide Types and Processes. Transportation Research Board, U.S. National Academy of Sciences, Special Report, 247: 36-75.

Dağdelenler G., Nefeslioğlu H.A., & Gökçeoğlu C. (2014). Landslide inventory of the eastern part of the Gallipoli Peninsula (Canakkale, Turkey). K. Sassa et al. (eds.), Landslide Science for a Safer Geoenvironment, Springer International Publishing, Switzerland, vol. 2.

Dağdelenler G., Nefeslioğlu H.A., & Gökçeoğlu C. (2015). Modification of seed cell sampling strategy for landslide susceptibility mapping: an application from the eastern part of the Gallipoli Peninsula (Çanakkale, Turkey). *Bulletin of Engineering Geology and the Environment*, 75, 575–590.

Dai S.K., Ling J.X., Chen Q.R., Li K., Zhang Q.J., Zhao D.D., & Zhang Y. (2021). Numerical modeling of 3D DC resistivity method in the mixed space-wavenumber domain. *Applied Geophysics*, 18, 361–374.

Di Giuseppe M.G., Troiano A., Fedele A., Caputo T., Patella D., Troise C., & De Natale G. (2015). Electrical resistivity tomography imaging of the near-surface structure of the Solfatara crater, Campi Flegrei (Naples, Italy). *Bulletin of Volcanology*, 77, 27.

Dimech A., Cheng L., Chouteau M., Chambers J., Uhlemann S., Wilkinson P., Meldrum P., Mary B., Fabien-Ouellet G., & Isabelle A. (2022). A Review on Applications of Time-Lapse Electrical Resistivity Tomography Over the Last 30 Years: Perspectives for Mining Waste Monitoring. *Surveys in Geophysics*, DOI: 10.1007/s10712-022-09731-2.

Drahor M.G., Göktürkler G., Berge M.A., & Kurtulmuş T.Ö. (2006). Application of electrical resistivity tomography technique for investigating landslides: a case from Turkey. *Environmental Geology*, 50, 147-155.

Duman T., Nefeslioğlu H.A., Can T., Ates S., Durmaz S., Olgun S., Hamzaçebi S., & Kecer M. (2006). Türkiye Heyelan Envanteri Haritası, 1/500.000 ölçekli İstanbul Paftası. Maden Tetkik ve Arama Genel Müdürlüğü (MTA - General Directorate of Mineral Research and Exploration of Turkey) Özel Yayınlar Serisi-6, Ankara, 25 s (In Turkish).

Emre, Ö., Duman, T.Y., Özalp, S., Elmacı, H., Olgun, Ş., & Şaroğlu, F. (2013). Active Fault Map of Turkey with Explanatory Text. MTA (General Directorate of Mineral Research and Exploration), Special Publication Series-30. Ankara-Turkey.

Fang H., Zhang H., Yao H., Allam A., Zigone D., Ben-Zion Y., Thurber C., & van der Hilst R.D. (2016). A new three-dimensional joint inversion algorithm of body-wave and surface-wave data and its application to the Southern California Plate Boundary Region. *Journal of Geophysical Research*, 121, 3557-3569.

Friedel S. (2003). Resolution, stability, and efficiency of resistivity tomography estimated from a generalized inverse approach. *Geophysical Journal International*, 153, 305-316.

Gökaşan E., Ergin M., Özyalvaç M., Sur H.I., Tur H., Görüm T., Ustaömer T., Batuk F.G., Alp H., Birkan H., Türker A., Gezgin E., & Özturan M. (2008). Factors controlling the morphological evolution of the Canakkale Strait (Dardanelles, Turkey). Geo-Marine Letters, 28, 107-129.

Gökaşan E., Görüm T., Tur H., & Batuk F. (2012). Morpho-tectonic evolution of the Çanakkale Basin (NW Anatolia): evidence for a recent tectonic inversion from transpression to transtension. *Geo-Marine Letters*, 32, 227–239.

Guo X., Huang X., & Jia Y. (2005). Forward modeling of different types of landslides with multi-electrode electric method. *Applied Geophysics*, 2, 14–20.

Hojat A., Arosio D., Ivanov V.I., Longoni L., Papini M., Scaioni M., Tresoldi G., & Zanzi L. (2019). Geoelectrical characterization and monitoring of slopes on a rainfall-triggered landslide simulator. *Journal of Applied Geophysics*, 170, 103844.

Karagöz Ö. (2022). Estimation of 1D Deep Vs Models in Çanakkale and Surrounding Area (Biga Peninsula, NW Turkey) Verified with Numerical Ground Motion Simulation of Moderate-Sized Earthquakes. *Pure and Applied Geophysics*, 179, 709–745.

Lai C.G., Bozzoni F., Conca D., Famà A., Özcebe A.G., Zuccolo E., Meisina C., Bonì R., Bordoni M., Cosentini R.M., Martelli L., Poggi V., Viana da Fonseca A., Ferreira C., Rios S., Cordeiro D., Ramos C., Molina-Gómez F., Coelho C., Logar J.,

Maček M., Oblak A., Ozcep F., Bozbey I., Oztoprak S., Sargin S., Aysal N., Oser C., & Kelesoglu M.K. (2020). Technical guidelines for the assessment of earthquake-induced liquefaction hazard at urban scale. *Bulletin of Earthquake Engineering*, 19, 4013–4057.

Lapenna V., & Perrone A. (2022). Time-Lapse Electrical Resistivity Tomography (TL-ERT) for Landslide Monitoring: Recent Advances and Future Directions. *Applied Sciences*, 12, 1425.

Li B., Xu Q., Cheng Q., Liu T.X., Tang M.G., Zheng G., & Wang H.Y. (2020). Characteristics of discontinuities in Heifangtai landslide area in Gansu, China. *Applied Geophysics*, 17, 857–869.

Loke M.H. (2004). Tutorial: 2-D and 3-D electrical imaging surveys. Geotomo Software, Penang, Malaysia.

MGM (2022). Meteoroloji Genel Müdürlügü (Turkish State Meteorological Service), Last visited October 15, 2022.

Milsom J. (2003). Field Geophysics. The Geological Field Guide Series, Third Edition, Willey, England.

MTA (2002). Geological map of Turkey (scale:1/500.000), MTA (General Directorate of Mineral Research and Exploration of Turkey) Publications, Last visited January 15, 2022.

MTA (2022). Turkey Landslide Inventory Map, MTA (General Directorate of Mineral Research and Exploration of Turkey) Publications, Last visited October 01, 2022.

MTA (2023). Active Fault Map of Turkey (scale:1/1.250.000). MTA (General Directorate of Mineral Research and Exploration of Turkey) Publications, Last visited March 12, 2023.

Naudet V., Revil A., Rizzo E., Bottero J.-Y., & Bégassat P. (2004). Groundwater redox conditions and conductivity in a contaminant plume from geoelectrical investigations. *Hydrology and Earth System Sciences*, 8, 8-22.

Okay A.I., Siyako M., & Burkan K.A. (1991). Geology and tectonic evolution of the Biga Peninsula. *Bulletin of the Technical University of Istanbul*, 44, 191–255.

Okay A.I., & Satır M. (2000). Upper Cretaceous eclogite facies metamorphic rocks from the Biga Peninsula, northwest Turkey. *Turkish Journal of Earth Sciences*, 9, 47–56.

Perrone A., Lapenna V., & Piscitelli S. (2014). Electrical resistivity tomography technique for landslide investigation: a review. *Earth-Science Reviews*, 135, 65-82.

Perinçek D. (2018). Geological and Geomorphological Analysis of the Ancient Erenköy and Güzelyalı Landslides in the Çanakkale District, NW Turkey. *Geological Bulletin of Turkey*, 61, 241-268 (In Turkish).

Ross D., Morrison M., Simyrdanis K., Roberts A., Moffat I., & The River Murray and Mallee Aboriginal Corporation (2019). A Geophysical Analysis of Aboriginal Earth Mounds in the Murray River Valley, South Australia. *Archaeological Prospection*, 26, 313–323.

Sağlık A., Domaç Y.S., Reyhan Ş.N., Avcı F., Kartal F., & Şenkuş D. (2021). Katı Atık Depolama Alanlarının Islahı ve Analizi Çanakkale Onsekiz Mart Üniversitesi Örneği. *Academia Journal of Nature and Human Sciences*, 7, 105-125 (In Turkish).

Saito H., Uchiyama S., Hayakawa Y.S., & Obanawa H. (2018). Landslides triggered by an earthquake and heavy rainfalls at Aso volcano, Japan, were detected by UAS and SfM-MVS photogrammetry. *Progress in Earth and Planetary Science*, 5, 15.

Sandikkaya, M.A. (2008). Site classification of Turkish national strong-motion recording sites. MS thesis, Middle East Technical University, Ankara.

Şaroğlu F., Emre Ö., & Kuşcu I. (1992). Active fault map of Turkey (scale: 1/1.000.000). MTA (General Directorate of Mineral Research and Exploration of Turkey) Publications.

Şengör A.M.C., Tüysüz O., Imren C., Sakınç M., Eyidoğan H., Görür N., Le Pichon X., & Rangin, C. (2005). The North Anatolian fault: A new look. *Annual Review of Earth and Planetary Sciences*, 33, 37-112.

Shao P, Shang Y, Hasan M, Yi X, & Meng H. (2021). Integration of ERT, IP, and SP Methods in Hard Rock Engineering. *Applied Sciences*, 11, 10752.

Su M., Cheng K., Liu Y., Xue Y., Wang P., Zhang K., & Li C. (2021). Combining geophysical methods, drilling, and monitoring techniques to investigate carbonaceous shale landslides along a railway line: a case study on Jiheng Railway, China. *Bulletin of Engineering Geology and the Environment*, 80, 7493–7506.

Sudha, K., Israil, M., Mittal, S., & Rai J. (2009). Soil characterization using electrical resistivity tomography and geotechnical investigations. *Journal of Applied Geophysics*, 67, 74-79.

Thirugnanam H., Uhlemann S., Reghunadh R., Ramesh M.V., & Rangan V.P. (2022). Review of Landslide Monitoring Techniques with IoT Integration Opportunities. *IEEE Journal of Selected Topics in Applied Earth Observations and Remote Sensing*, 15, 5317-5338.

Travelletti J., & Malet J.-P. (2012). Characterization of the 3D geometry of flow-like landslides: a methodology based on the integration of multisource data. *Engineering Geology*, 128, 30-48.

Xia, J., Miller, R.D., & Park, C.B. (1999). Estimation of near-surface shear-wave velocity by inversion of Rayleigh waves. Geophysics, 64, 691–700.

Xu D., Hu X.Y., Shan C.L., & Li R.H. (2016). Landslide monitoring in southwestern China via time-

lapse electrical resistivity tomography. *Applied Geophysics*, 13, 1–12.

Yaltırak C., Alpar B., Sakınç M., & Yüce H. (2000). Origin of the Strait of Çanakkale (Dardanelles): regional tectonics and the Mediterranean – Marmara incursion. *Marine Geology*, 164, 139–156, with erratum 167, 189–190.